https://doi.org/10.5194/egusphere-2026-2373
Preprint. Discussion started: 5 June 2026

Method for near real-time detection of snow avalanches using Distributed Acoustic Sensing

Pascal Edme[1], Cristina Pérez-Guillén[3], Alec Van Herwijnen[3], Johannes Aichele[1], Andri Simeon[3], Patrick Paitz[2], Fabian Walter[2], and Andreas Fichtner[1]

[1]Institute of Geophysics, ETH Zurich, Zurich, Switzerland
[2]Swiss Federal Institute for Forest, Snow and Landscape Research WSL, Birmensdorf, Switzerland
[3]WSL Institute for Snow and Avalanche Research SLF, Davos, Switzerland

Correspondence: Pascal Edme (pascal.edme@eaps.ethz.ch)

Abstract. We present a novel method for near real-time snow avalanche detection using Distributed Acoustic Sensing (DAS). A ∼10 km long telecommunication cable permanently installed along the avalanche-prone Flüelapass road (Swiss Alps) was continuously monitored over a full winter. Avalanches, including events that did not physically reach the cable, were clearly recorded and confirmed with photographic evidence. To discriminate avalanches from anthropogenic signals, we introduce a dual-frequency short-term over long-term average attribute that produces coherent high-value spatio-temporal signatures for avalanches, while vehicles predominantly generate negative values with pronounced move-out. The workflow consists of (1) a quasi-instantaneous threshold-based trigger to detect onset time and location, followed by (2) a rapid waterfall image analysis to estimate event extent and invalidate traffic-induced alerts. The first step issues alerts with millisecond-scale latency and meter-scale spatial resolution. The second step introduces additional latency, as it requires the event to sufficiently develop in order to assess its spatio-temporal morphology and confirm or discard the initial trigger. Our system issued alerts only 4.5 ‰ of the time when the road pass was open (i.e. 2.5 hours over 23 days), demonstrating the robustness against traffic, and 0.36 ‰ of the time when the pass was closed (i.e. 55 minutes over 108 days). Among those, a total of 73 potential avalanches were identified, most of them occurring during three independently documented avalanche episodes. These findings demonstrate that DAS represents a viable and cost-effective solution for operational real-time avalanche monitoring, with potential applicability to broader natural hazard detection.

1 Introduction

Mass movements represent an increasing hazard to populations and critical infrastructure worldwide (Stoffel and Huggel, 2012; Chiarle et al., 2021; Eckert et al., 2024). Landslides, avalanches and flash floods frequently pose a significant risk to the population, with thousands of fatalities each year and billions of dollars in financial damage (Dilley, 2005; Petley, 2012; Froude and Petley, 2018; Emberson et al., 2020). In Switzerland, snow avalanches represent the deadliest natural hazards (Badoux et al., 2016), having the potential to cause economic losses over several hundreds of millions of Swiss Francs (Bründl et al., 2004). Avalanche monitoring is an active area of research (Denissova et al., 2024), and mitigation measures have been implemented in the Swiss Alps for many years (Fuchs et al., 2007). However, while permanent mitigation measures such as structural protection and land-use planning can substantially reduce avalanche risk, they are costly and not always feasible for all exposed infrastructure. In many situations, risk management therefore relies on temporary measures such as road closures and evacuations. These measures require timely and reliable information on avalanche occurrence, highlighting the need for robust avalanche detection systems.

To date, ground-based operational monitoring systems rely mainly on optical and radar observations (Eckerstorfer et al., 2016; Köhler et al., 2018, 2020; Gauer et al., 2007; Caduff et al., 2015), impact measurements (Baroudi et al., 2011), as well as infrasound (Marchetti et al., 2015; Mayer et al., 2020) and seismic sensors (Allstadt et al., 2018; Hürlimann et al., 2019; Simeon et al., 2025). Impact measurements (e.g., by tripwires) are by definition installed in situ, which limits deployment to particular avalanche paths on well-known slopes. In contrast, ground-based remote sensing methods cover a larger investigation area. Passive optical methods such as time-lapse photography and photogrammetry can provide near-real time data, but are limited by sensor illumination and exposure, making them highly dependent on season, weather and the diurnal cycle. Ground-based radars comprise Doppler- and Interferometric methods, which allow retrieving previously unprecedented spatio-temporal resolution of avalanche dynamics (Köhler et al., 2016). Radars are employed to guide for example road closures (Meier et al., 2016). These active and passive remote sensing techniques are limited to a device and topography-dependent field-of-view, resulting in limited spatial coverage.

Ground-based systems that are neither slope-specific nor weather-dependent include infrasound and seismic sensors. The former measure acoustic waves propagating in air and snow while the latter measure elastic waves propagating in snow and solid subsurface. Both methods have been used to detect and characterize mass movements, e.g. (Suriñach et al., 2005; Schimmel et al., 2018). Infrasound sensors can be installed in a snow avalanche path or in the valley for monitoring and dynamic characterization (Sovilla et al., 2025). By employing microphone arrays, avalanche path and kinematics can be deduced (Marchetti et al., 2015). Similar to infrasound, seismic sensors can be employed in the seismic near-field (Vilajosana et al., 2007; Van Herwijnen and Schweizer, 2011; Pérez- Guillén et al., 2016) and far-field (Lawrence and Williams, 1976; Hammer et al., 2017). Measurements of up to 15 km from the avalanche have been reported (Lacroix et al., 2012; Pérez-Guillén et al., 2019; Hammer et al., 2017). Developments include automated array processing for localization and characterization (Lacroix and Helmstetter, 2011; Lacroix et al., 2012) and machine learning to further improve detection and warning capabilities for mass movements (Chmiel et al., 2021; Kang et al., 2024; Heck et al., 2019a).

Seismic systems stand out for their ability to provide continuous monitoring across wide areas regardless of visibility conditions (Pérez- Guillén et al., 2016; Simeon et al., 2025). However, the installation and maintenance of dense arrays of conventional seismic sensors in alpine terrain is challenging and costly. Moreover, limitations remain in both spatial resolution and coverage (Dietze et al., 2017; Heck et al., 2019b). Robust real-time detection requires further extensive, large-scale monitoring solutions (Mayer et al., 2020), complementing systems that are either highly site-specific or air- and space-borne (Eckerstorfer et al., 2016).

Fiber-optic sensing, and in particular Distributed Acoustic Sensing (DAS), may address those issues. DAS has recently emerged as an alternative seismic data acquisition technology that offers dense spatial coverage with significantly lower cost and effort, by transforming any standard telecommunication optical fiber into a very large number of ground deformation sensors with a

https://doi.org/10.5194/egusphere-2026-2373
Preprint. Discussion started: 5 June 2026

meter scale sampling (Hartog, 2017; Lindsey and Martin, 2021). The DAS system consists of an Interrogation Unit (IU) that emits and receives laser pulses in a fiber-optic cable. Hence, a single instrument forms a high-resolution distributed sensing antenna potentially over several tens of kilometers, making large-scale real-time monitoring logistically feasible and cost-effective. The DAS instrument response has been studied over a wide range of frequencies (Lindsey et al., 2020; Paitz et al., 2020), and the sensitivity of current IUs has opened new opportunities in cryosphere research (Walter et al., 2020; Klaasen et al., 2021; Brisbourne et al., 2021; Hudson et al., 2021; Fichtner et al., 2022; Booth et al., 2020; Fichtner et al., 2023; Booth et al., 2023; Fichtner et al., 2025) and in avalanche studies in particular (Prokop et al., 2014; Paitz et al., 2023; Turquet et al., 2024).

The application of DAS systems for real-time avalanche detection still remains sparse (Barla et al., 2025; Kleine et al., 2025). Here we present the results from a DAS experiment using a fiber in a telecommunication cable along a mountain pass road in Switzerland. The cable crosses several avalanche-prone sections, providing a commonly encountered dangerous situation that demands monitoring and warning solutions. In this paper, we propose an approach to efficiently distinguish avalanches from most anthropogenic noises such as vehicles. The method is designed to trigger alerts with minimal latency.

2 Experimental setup and phenomenology

2.1 Interrogation setup

From December 23rd 2021 to May 9th 2022, we interrogated a ∼10 km long existing fiber-optic telecom cable along the Flüelapass, a high mountain pass road in the eastern Swiss Alps (Fig. 1a). The elevation profile ranges from 1414 to 2181 m above sea level. The site is well-known for the frequent natural release of snow avalanches. Different sections of the road are exposed to high avalanche hazard, as shown in Fig. 1a), and it is consequently closed to the public during the winter season for three to four months per year.

Fig. 1 shows the trajectory of the fiber-optic cable in yellow. The approximate geometry was provided by Swisscom Broadcast and the locations of the DAS channels were further identified through tap tests on-site, leading to an estimated precision of ∼20 m. The DAS interrogator (a Silixa iDAS^{TM} 2.0 using a fixed 10 m gauge length) was located in the basement of a Swisscom fiber distribution hub in the village of Susch. The first ∼3 km of fiber traversed populated areas and were not analyzed in this study. The cable then closely follows the mountain pass road from ∼3 km to ∼6 km fiber distance. For the upper ∼4 km (Fig. 1b), it follows the south side of the Susasca River in the valley, with a maximum distance of ∼400 m from the road. The data were initially acquired with a sampling frequency of 200 Hz and 10 m channel spacing. Based on preliminary analyses, we decided on January 21st to reduce the sampling rate to 100 Hz and record with a denser spatial sampling of 2 m, resulting in ∼5000 channels. To homogenize the acquisition and accelerate further processing, the entire dataset was later resampled to 50 Hz and 6 m, resulting in a manageable volume of 1.8 TB. In order to validate potential avalanche records with ground-truth observations, we performed several field visits, installed a camera near the top of the cable (see Fig. 1b) and used a drone to collect photographic evidence. As additional assessment tool, we also simulated the evolution of the snow stratigraphy and liquid water content using the physics-based, multi-layer SNOWPACK model (Lehning et al., 2002; Bartelt

https://doi.org/10.5194/egusphere-2026-2373
Preprint. Discussion started: 5 June 2026

a) Avalanche terrain hazard map of the Flüelapass

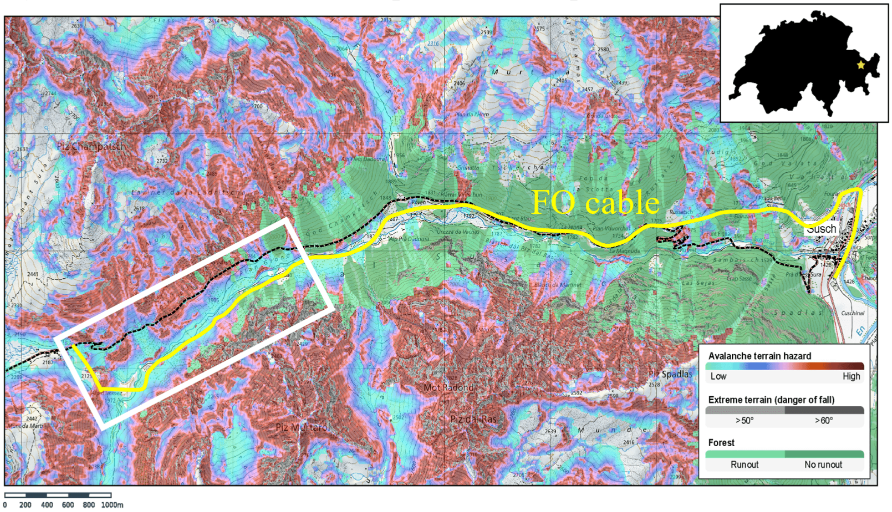

b) Top 4 km of the monitored fiber-optic cable

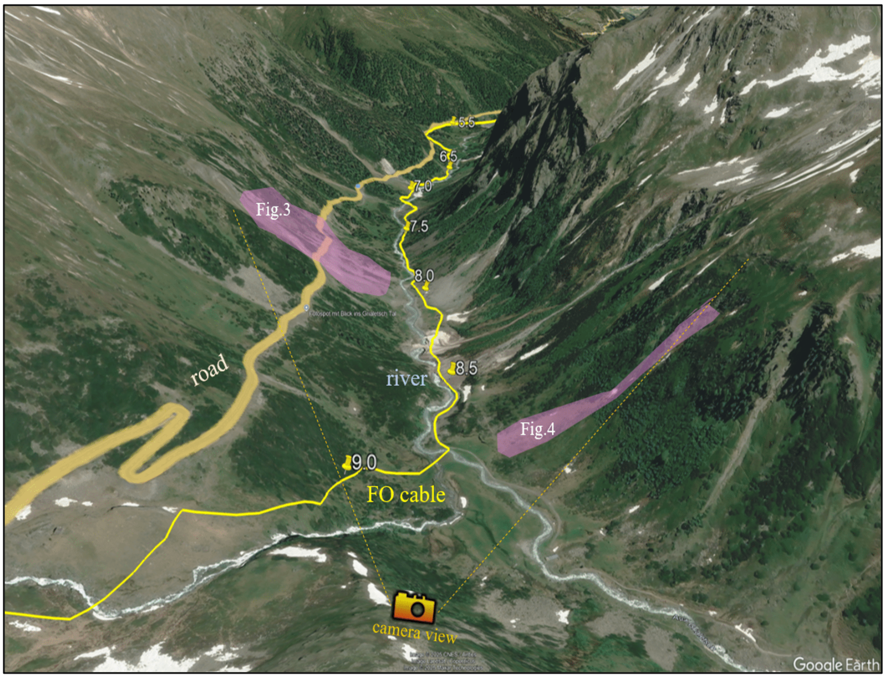

Figure 1. a) Avalanche terrain hazard map (from White Risk platform, https://whiterisk.ch/en/welcome) of the monitored Flüelapass road (dashed black curve). The map shows the release areas, runout zones, and danger of avalanches: the higher the value (red), the greater the avalanche hazard. Extremely steep terrain is coloured grey, and forest is green. The telecommunication cable (in yellow) starts from Susch and leads up to the pass top (km 10). The fiber initially follows the road up to ∼6 km distance then remains close to the Susasca River. b) Top part of the site (i.e., last 4 km of cable), where most of the avalanche activity takes place. Yellow pins indicate cable distances (in km) from the DAS interrogator. The two pink areas indicate the locations of the avalanche examples shown in Figs. 3 and 4 (the latter having been captured with the camera approximately located as illustrated here in orange). Maps data: © Google Earth 2025; images: © CNES/Airbus, Maxar Technologies, Airbus.

https://doi.org/10.5194/egusphere-2026-2373
Preprint. Discussion started: 5 June 2026

and Lehning, 2002) driven by input weather data from two nearby meteorological stations at 2677 m and 1563 m above sea level. Finally observations were collected across Switzerland by SLF observers, recreational backcountry users, and automatic detection systems operated by different Swiss companies via the SLFPro platform (https://pro.slf.ch/workbench), providing a supplementary avalanche database for further validation.

2.2 Data overview

This section provides a low-resolution overview of the complete dataset, with Fig. 2 showing attributes independently computed for individual DAS channels over consecutive five-minute time windows (as per 50 Hz resampled file length).

Fig. 2a depicts the mean absolute value of the measured strain rate, highlighting the background ambient noise. It can be observed that the adjustment in the acquisition setup implemented on January 21st resulted in a reduced noise level. We also observe that noise levels rise toward the end of the season, a pattern we attribute to snowmelt whose onset varies significantly with elevation. For instance, simulations of Fig. A1a and A1b indicate that the entire snowpack became completely wet (with liquid water content greater than or equal to 3%) about one month earlier (mid-March) at 1563 m a.s.l. (Davos weather station) than at 2677 m a.s.l. (Zernez weather station).

Fig. 2b shows the strain rate standard deviation of the same envelope, accentuating time windows containing significant fluctuations, and therefore indicative of events (e.g., water discharge detected at the pedestrian bridge at $\sim$7 km distance). This metric further reveals the vehicle traffic along the road (distances from 3 km to 6 km highlighted in Fig. 2c) when the pass was open. The activity at $<$1.5 km is mostly car traffic on the cantonal road through the Engadin valley, which is not affected by winter closure of the Flüelapass road.

Fig. 2c shows the coefficient of variation highlighting time windows containing transient events, even amidst increasing noise levels. We found this metric particularly effective for detecting seismic activity, even of modest amplitude. Its detailed inspection reveals a wide range of signals, which we will further discuss in the next sections. For example, the close-up in panel c) highlights a period of avalanche activity, with multiple wet-snow avalanches occurring on April 15th (e.g., Fig. 4, as detailed in Section 2.3). The primary challenge lies in distinguishing avalanches from various anthropogenic noise sources, in particular vehicle traffic.

2.3 Signal examples

The first step in identifying potential avalanche events in the recordings was a visual inspection of the data, as shown in the selected examples of Figs. 3 and 4. Subsequently, we used field observations to confirm individual avalanche events. For instance, drone images acquired on March 25th enabled us to confirm an avalanche that had released six days earlier and had crossed the mountain pass road at approximately 8 km along the fiber. The event is shown in Fig. 3, with a resulting DAS signal lasting approximately 30 s and distinguishable over more than 1 km along the fiber, despite its visible physical extent being less than 300 m. The snow mass stopped at the bottom of the valley on the north side of the river and therefore did not propagate over the cable located slightly higher on the south side.

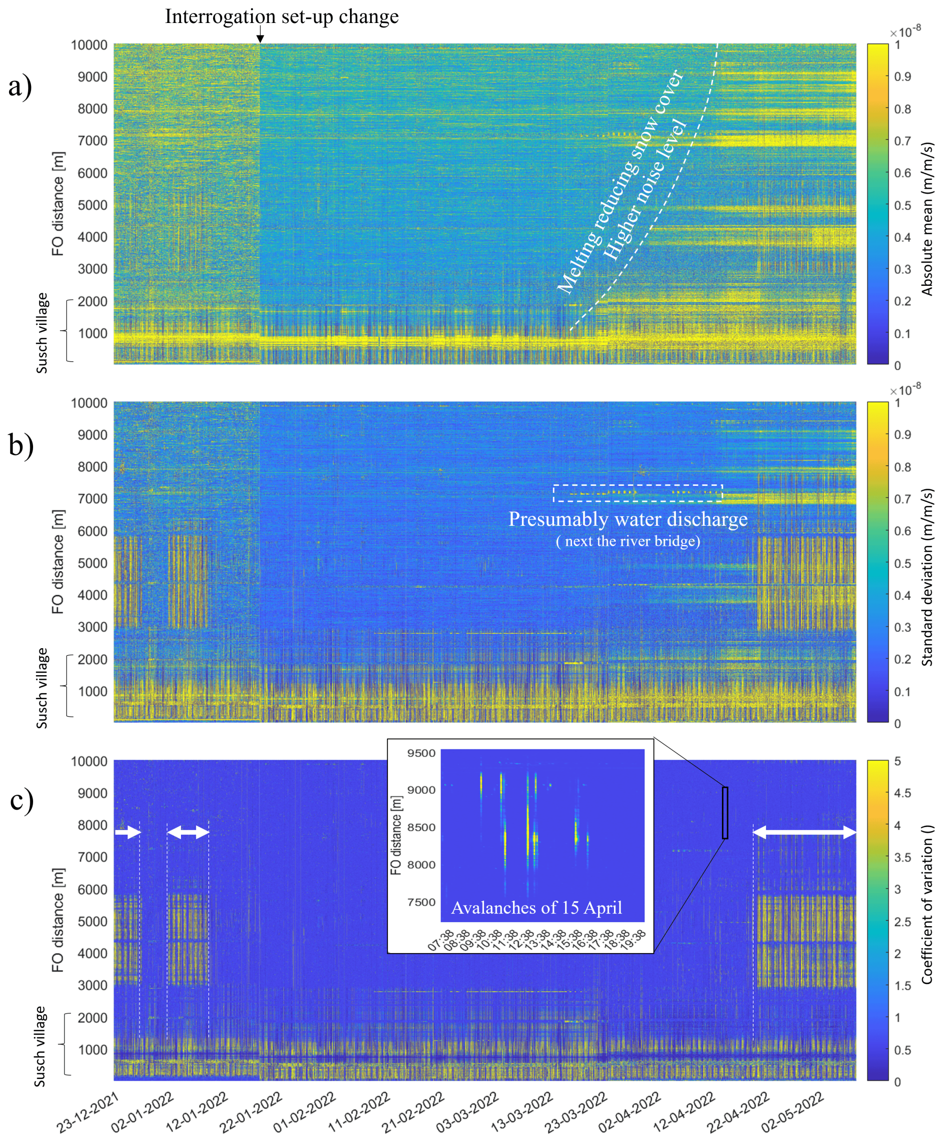

Figure 2. Dataset overview, with attributes independently calculated over the envelope of the signal, per channel and per 5 minutes long time intervals. a) Mean absolute value of the envelope. b) Standard deviation of the envelope. c) coefficient of variation (i.e., ratio of b) over a)). White arrows in panel c) indicate periods of time when the pass remained open to traffic. The zoomed time window on April 15th reveals clear events, which we could confirmed to be wet snow avalanches.

https://doi.org/10.5194/egusphere-2026-2373
Preprint. Discussion started: 5 June 2026

a) Photograph of a large avalanche released on March 19th 2022, crossing the road

b) DAS recording along the complete cable

c) Zoom into the avalanche

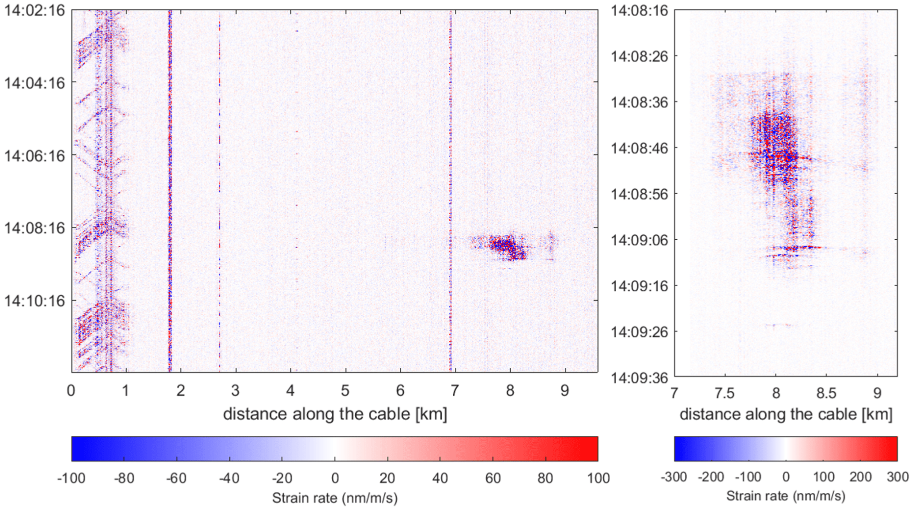

Figure 3. Example of an avalanche that released on March 19th, traversing the Flüelapass road and reaching the Susasca river in the valley (opposite the cable location). a) Drone image taken 6 days after the event. b) DAS recording along the complete ∼10 km long fiber-optic cable. Recordings at <1 km are mostly cars in the village of Susch. c) Zoom into the snow avalanche recording, showing clear signal over ∼1.5 km, in between ∼7.5 and ∼9 km distance from the interrogator.

https://doi.org/10.5194/egusphere-2026-2373
Preprint. Discussion started: 5 June 2026

a) Photograph of a wet avalanche on April 15th 2022

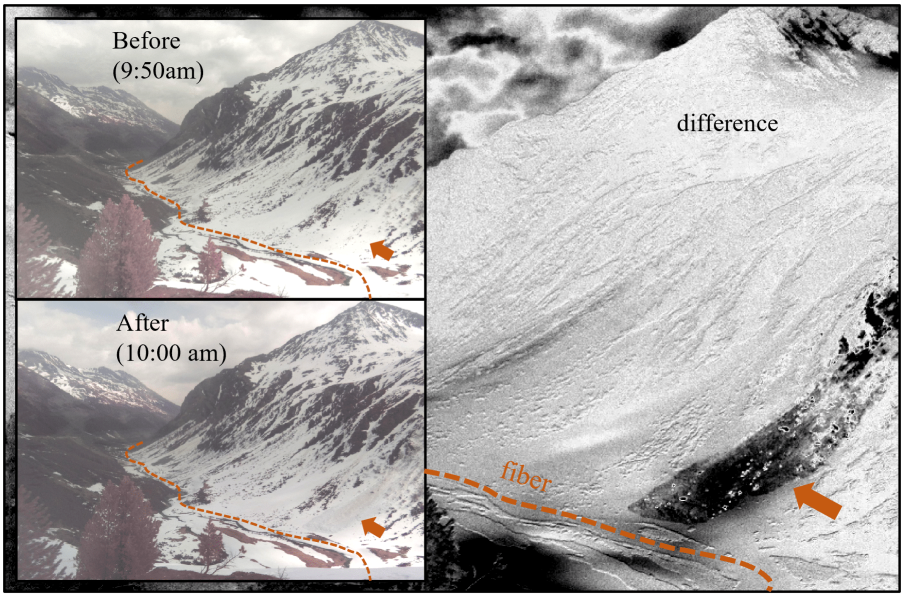

b) DAS recording along the complete cable

c) Zoom into the avalanche

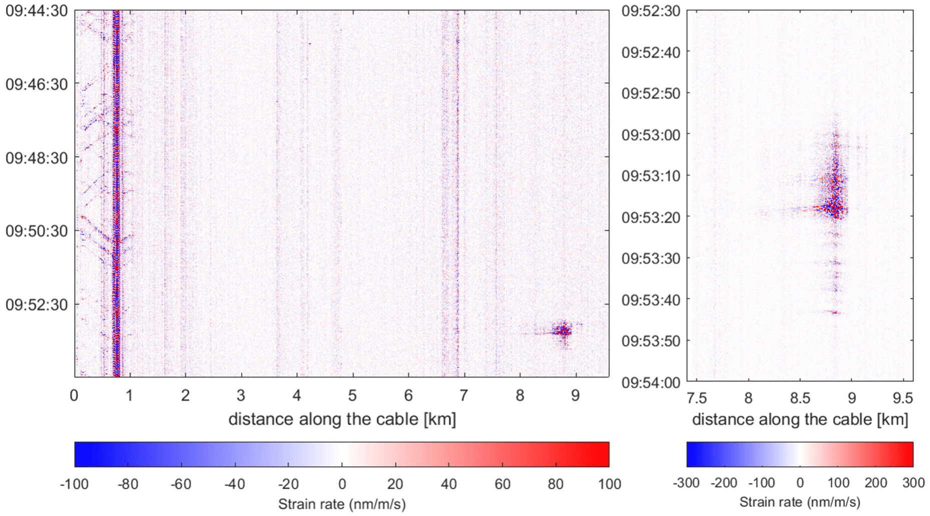

Figure 4. Example of a snow avalanche that released on April 15th. a) Photographs taken before and after the event (10 min interval). Shown in gray scale is the contrast-boosted difference between the two raw pictures, with the arrow indicating the avalanche deposit. b) DAS recording along the complete ∼10 km long fiber-optic cable. c) Zoom into the snow avalanche recording, with clear signals around 8.8 km (± 200 m) and lasting ∼50 s.

https://doi.org/10.5194/egusphere-2026-2373
Preprint. Discussion started: 5 June 2026

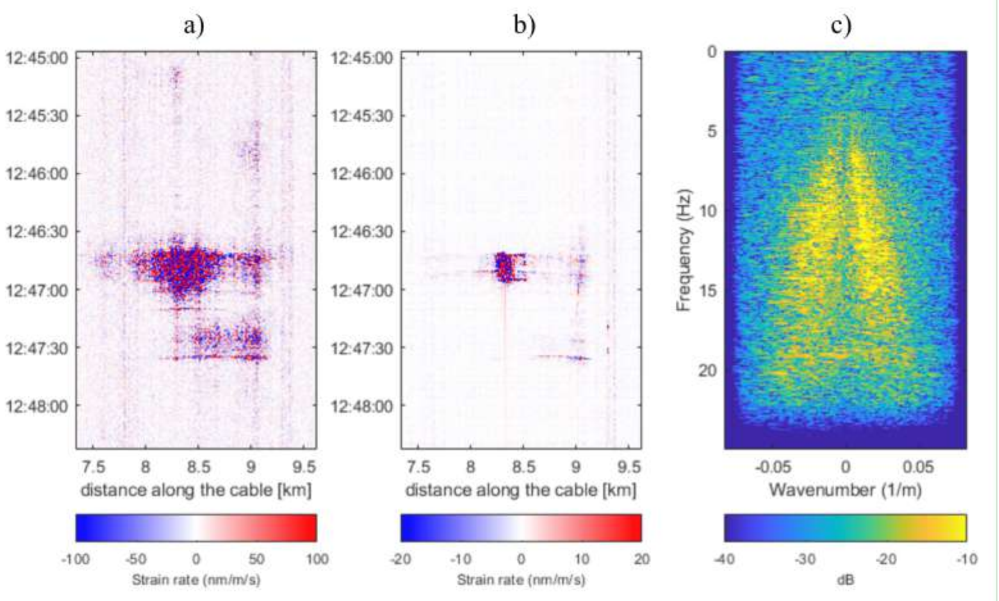

Figure 5. Example of a wet snow avalanche that occurred in the early afternoon of the April 15th. a) Full bandwidth up to 25 Hz. b) Low-pass filtered version using a Chebyshev operator (-20 dB at 5 Hz, -100 dB beyond 8 Hz). Note the weaker amplitude of the lower frequencies, which are also visible over a smaller spatial extent than the higher frequencies. c) f-k domain spectrum, further highlighting the high frequency (>5 Hz) dominance.

Later in the season, using images from an automatic camera installed at the end of the fiber-optic cable, we confirmed other avalanches that released on April 15th. One example is shown in Fig. 4. Despite its occurrence on the south side of the river, this relatively small avalanche did not reach the fiber and stopped approximately 20 m before it. The event is still visible over a few hundred meters in the DAS data, with induced strain rate fluctuations reaching 3 $\mu m/m/s$.

Fig. 5 shows another avalanche that released on April 15th. Panel a) displays the full bandwidth up to 25 Hz, while panel b) shows its low-pass filtered version under 5 Hz. The corresponding frequency-wavenumber (f-k) spectrum displayed in panel c) does not reveal clear modes, as expected from the complex signals in the time-space domain. The f-k plot highlights that the wavefield is largely dominated by frequencies above 5 Hz and we will demonstrate that the weak low frequency component can be useful to discriminate avalanches from signals of other origins. For example, vehicle traffic signals (recorded between 3 and 6 km distances) result in a distinct f-k content (see Fig. 6), with a relatively clear mode under 2 Hz. While this observation alone could potentially serve as a basis for avalanche discrimination, we identified a more robust diagnostic feature for this purpose, as described in Section 3. Moreover, a meaningful interpretation of the f–k transform requires processing straight fiber segments, and this method is computationally too expensive for real-time analysis since it requires processing small sliding time–space windows.

https://doi.org/10.5194/egusphere-2026-2373
Preprint. Discussion started: 5 June 2026

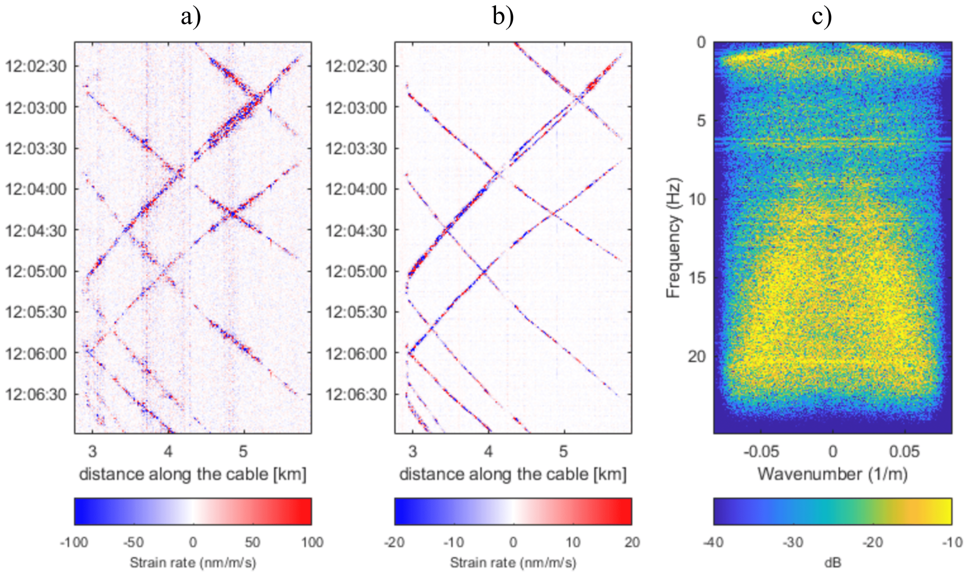

Figure 6. Example of car traffic DAS signals (5 minutes long record) while the pass was open. a) Full bandwidth up to 25 Hz. b) Low-pass filtered version (same operator as in Fig. 5). c) f-k domain spectrum.

3 Proposed automatic avalanche detection algorithm

Detecting snow avalanches in real-time with minimal latency and false alerts amidst the numerous other events poses a significant challenge. We opted for an empirical detection approach rather than a machine-learning model to prioritize interpretability, and reproducibility. The resulting algorithm emerged from iterative inspection and testing, guided by careful signal analysis and implemented with tools optimized for real-time processing under limited computational resources.

3.1 STA/LTA analysis

Our solution to discriminate avalanches from other events arose from the observation of the short-term average (STA) over the long-term average (LTA) ratio considering different spectral content. Given the volume of data and the need for a simple and efficient algorithm, the well-known STA/LTA approach (Allen, 1978; Withers et al., 1998) was an obvious option to detect potentially weak signals under fluctuating background noise conditions. The characteristic function $\sigma(t)$ is typically computed as follows:

$$\sigma(t) = \frac{\mathrm{STA}(t)}{\mathrm{LTA}(t)} = \frac{\frac{1}{N}\sum\limits_{i=t-N}^{t}\epsilon_i^2}{\frac{1}{M}\sum\limits_{i=t-M}^{t}\epsilon_i^2}, \tag{1}$$

where ϵ_i is the DAS strain rate sample at time index i, while N and M denote the number of time samples used for the short-term and long-term averaging, respectively. The characteristic function $\sigma(t)$ becomes available after a waiting (or readiness) time of M samples, but is then dynamically updated with every newly collected time sample. Although computed channel per channel, the process is fast enough to be applied over the whole cable in real-time, without introducing any latency. Fig. 7a shows the typical $\sigma(t)$ response obtained from Eq. (1) for a single channel (at distance 8953 m within the records of Fig. 4). This example highlights several key characteristics: the $\sigma(t)$ attribute (i) initially oscillates around 1 when the signal is dominated by noise, (ii) rapidly increases above 2 as soon as some energy is present in the short-term window (millisecond-scale latency), (iii) decreases when more energy accumulates in the long-term window, (iv) approaches zero when little or no energy is within the short-term window but remains significant within the long-term one, and (v) finally returns to its initial state, fluctuating around 1.

In brief, $\sigma(t)$ is effective in highlighting transient events, including those of small amplitude, as long as they are above the noise floor. By relying solely on causal samples, such a detector operates with low latency, with event onset identified as soon as the short-term average dominates the long-term background level. Another advantage is that $\sigma(t)$ remains close to 1 in the absence of transient events, irrespective of the fluctuating background strain rate noise levels.

3.2 Detection feature: dual frequency STA/LTA combination

We propose to exploit the characteristic function $\sigma(t)$ computed over two frequency bands to highlight both the weaker and slower nature of the low-frequency component of the seismo-acoustic wavefield generated by snow-avalanches. This approach is illustrated in Figs. 7 and 8, presenting an avalanche and a car traffic example, respectively. In both cases, panel a) shows $\sigma(t)$ derived from the full-bandwidth data (below 25 Hz), while panel b) displays the low-frequency version (below 5 Hz, obtained by convolution with a Chebyshev operator), hereafter denoted $\sigma_{\mathrm{LF}}(t)$.

In the avalanche example (Fig. 7), the full-band $\sigma(t)$ highlights three main surges or events. In comparison, $\sigma_{\mathrm{LF}}(t)$ shows slightly delayed and weaker peaks for the two main events at approximately 160 s and 200 s. The first event, at around 105 s, completely lacks low-frequency energy. This behavior contrasts with the car traffic example (Fig. 8), in which all events produce $\sigma_{\mathrm{LF}}(t)$ peaks of similar strength and timing as those in the full-band $\sigma(t)$.

Another key difference is that, in the car example, $\sigma_{\mathrm{LF}}(t)$ does not exhibit any noticeable time lag relative to the full-band signal. This can be explained by the fact that, although car-generated surface waves are dispersive, the frequency components do not separate temporally when measured by a nearby cable. In contrast, avalanches generate higher-frequency signals preceding lower-frequency components. This relative time delay, observable by comparing $\sigma(t)$ and $\sigma_{\mathrm{LF}}(t)$, forms our central feature for discriminating avalanche signals.

A simple way to assess this delay could be through direct $\sigma(t) - \sigma_{\mathrm{LF}}(t)$ subtraction, as shown by the pink curves in Figs. 7c and 8c: car signals typically result in sharp troughs, while avalanche events produce broader, high-amplitude peaks lasting several seconds. While such a difference could in principle support threshold-based triggering for avalanche detection, a challenge arises from occasional spikes in car signals, such as the one around 90 s in Fig. 8c that could be misinterpreted as avalanche activity. To address this and leverage the fact that vehicles travel at much lower speeds than seismic waves, we propose a more

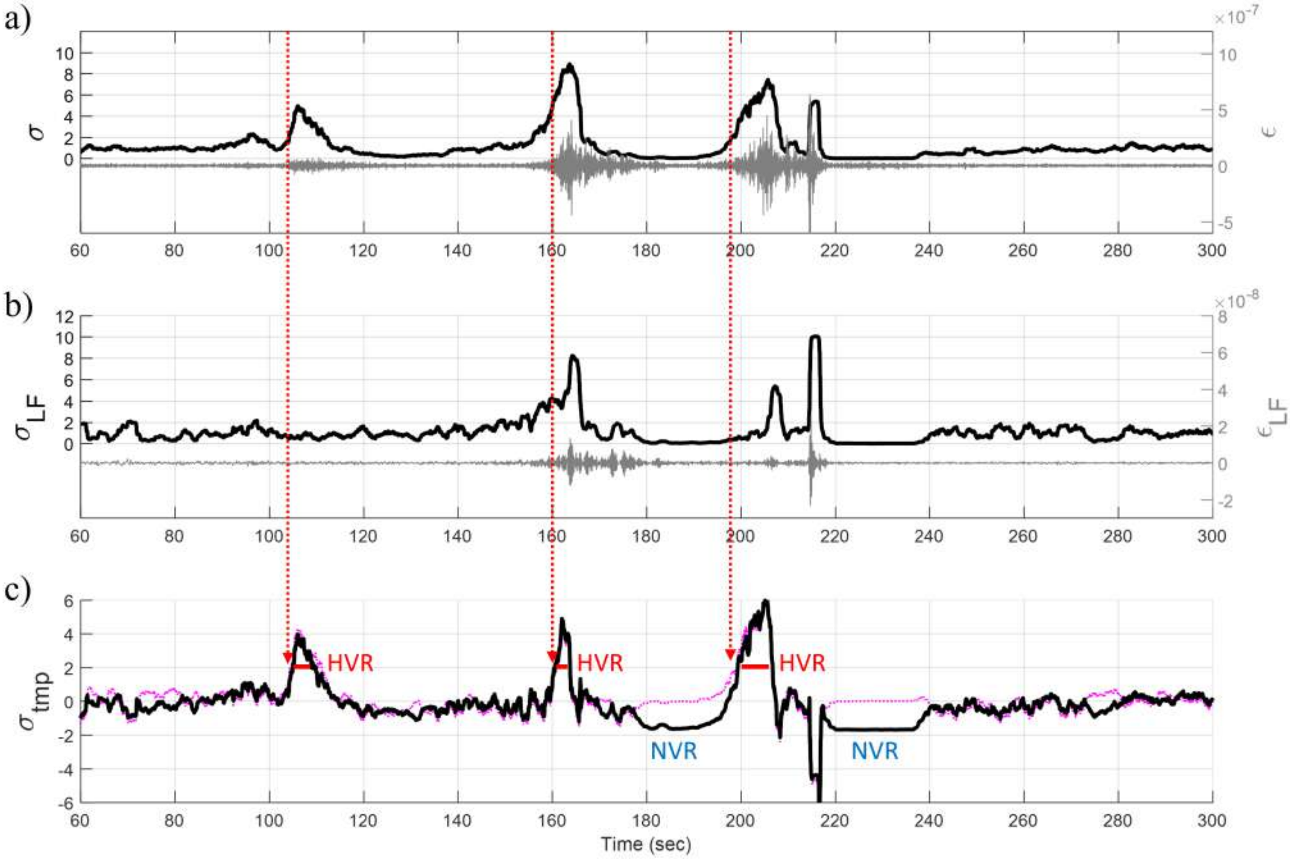

Figure 7. STA/LTA example for a DAS channel at 8941 m from the avalanche recording of Fig. 5. a) $\sigma(t)$ (black) of the full-bandwidth data (gray). b) $\sigma_{\mathrm{LF}}(t)$ (black) for filtered data at frequencies < 5 Hz (gray). c) The temporary attribute $\sigma_{\mathrm{tmp}}(t)$ resulting from Eq. (2). The three avalanche surges exhibit clear spikes (high value regions HVR, in red), potentially followed by a negative value region (NVR, in blue). The dashed pink curve shows the result of a plain subtraction between $\sigma(t)$ and $\sigma_{\mathrm{LF}}(t)$, providing comparable output as $\sigma_{\mathrm{tmp}}(t)$ but without the NVR. Here, based on trial-and-error tuning, we used short- and long-term windows of 2 s and 20 s, respectively.

https://doi.org/10.5194/egusphere-2026-2373
Preprint. Discussion started: 5 June 2026

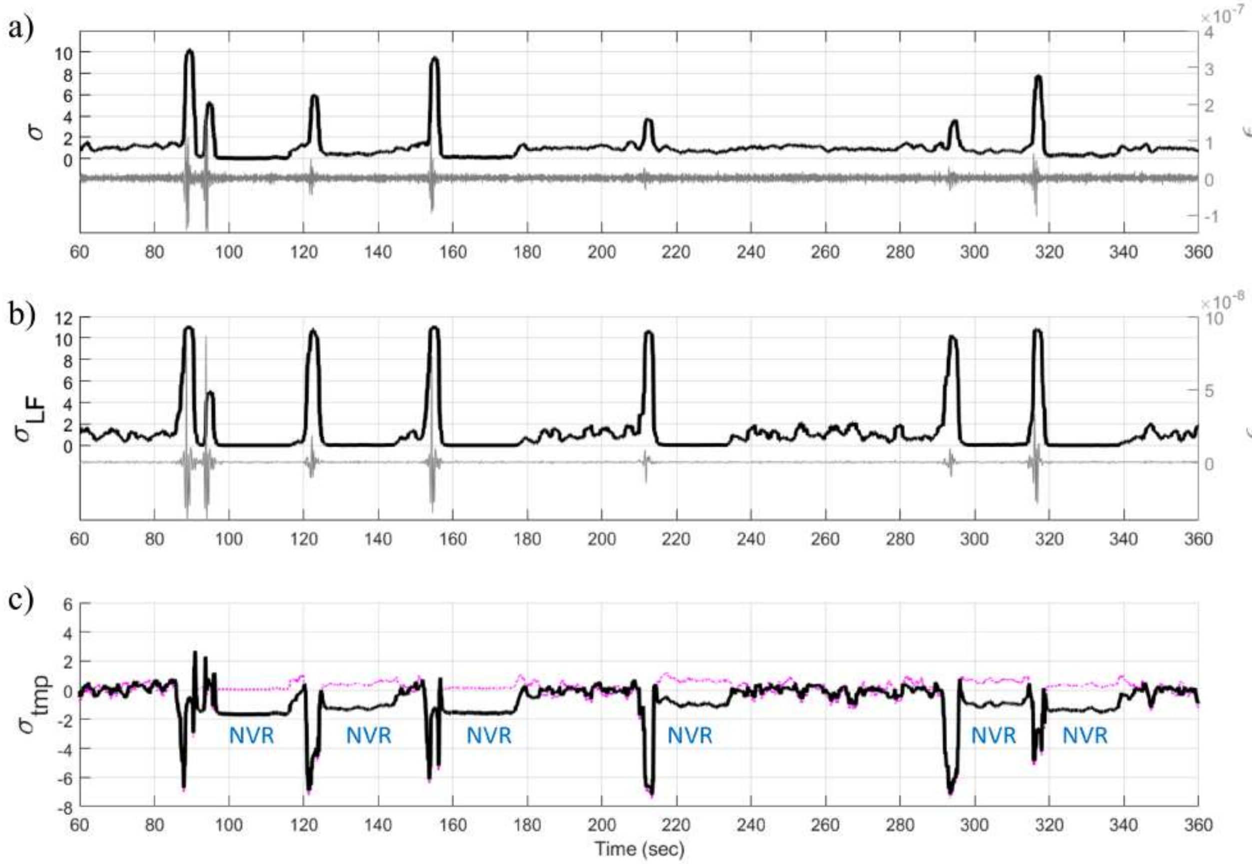

Figure 8. Same as Fig. 7 but now applying the process on a DAS channel at 4453 m from the traffic recording of Fig. 6. With cars, $\sigma_{\mathrm{tmp}}(t)$ outputs mostly NVRs, without HVRs. The plain subtraction (in pink) between $\sigma(t)$ and $\sigma_{\mathrm{LF}}(t)$ would be fluctuating noise around zero, without NVRs, as opposed to $\sigma_{\mathrm{tmp}}(t)$ (in black) obtained via Eq. (2). This figure highlights that a simple STA/LTA would trigger for each individual cars, in contrast to our proposed dual-frequency approach.

robust combination of the dual-frequency σ signals:

$$\sigma_{\text{tmp}}(t) = \sigma(t) - |\sigma_{\text{LF}}(t) - 1| - 1/\sqrt{2} \tag{2}$$

where the term $1/\sqrt{2}$ serves to detrend the output so that $\sigma_{\text{tmp}}(t)$ fluctuates around zero when the data are dominated by ambient noise. The key ingredient here is the introduction of the $|\sigma_{\text{LF}}(t) - 1|$ subtraction, which aims at emphasizing the situation when both $\sigma(t)$ and $\sigma_{\text{LF}}(t)$ are closed to zero, i.e., when the long-term window energy dominates over the short-term fluctuations. As shown in Figs. 7c and 8c, compared to plain subtraction, the combination defined in Eq. 2 preserves the overall response in terms of spikes (hereafter referred to as high-value regions, HVRs), but introduces pronounced negative-value regions (NVRs) in intervals where the LTA clearly dominates the STA. In the traffic example in particular, this produces a distinctive pattern of extended NVRs trailing the onset of car-generated signals. When this process is applied across all DAS channels, yielding $\sigma_{\text{tmp}}(t, \forall x)$ where x denotes channel location, these NVRs can be exploited to suppress undesirable traffic-induced local spikes. This effect is illustrated in Figs. 9 and 10, where panels a) display the $\sigma_{\text{tmp}}(t, \forall x)$ attribute. Although vehicle signals may occasionally produce relatively high σ_{tmp} values, their spikes are typically weaker and more spatially scattered than those associated with avalanche events. Moreover, due to the significant move-out characteristic of vehicle traffic signals, the resulting NVRs tend to be spatially adjacent to the corresponding HVRs. This spatial relationship can be leveraged to further attenuate "spurious" spikes using a simple smoothing strategy, namely a spatial moving median filter: ’

$$\sigma_{\text{trig}}(t,x) = \text{median}[\sigma_{\text{tmp}}(t, x-k), \ldots, \sigma_{\text{tmp}}(t,x), \ldots, \sigma_{\text{tmp}}(t, x+k)], \tag{3}$$

where k is the half-length of the moving median filter. This procedure, suitable for real-time applications, introduces no latency. The resulting $\sigma_{\text{trig}}(t, \forall x)$ attribute is shown in Figs. 9b and 10b, using k = 360 m. This simple spatial filtering step effectively attenuates undesired HVRs within the traffic signal while preserving clear and distinct HVRs associated with avalanche events. In contrast to the traffic example, the σ_{trig} attribute in the avalanche case exhibits high values even for weak events that are barely visible in the raw strain-rate data (e.g., at 12:45:02 and 12:45:32). This demonstrates the algorithm’s capability to detect small-size avalanches of interest.

In summary, we demonstrate that the NVR regions introduced via Eqs. 2 and 3 facilitate the identification and suppression of car-induced signals while simultaneously producing a distinct signature for avalanche events. As illustrated in Fig. 9b, the σ_{trig} attribute typically yields broad, flat HVRs, often followed by slightly narrower NVRs when the avalanche produces significant low-frequency content. In contrast, as shown in Fig. 10b, vehicle traffic generally results in NVRs characterized by greater move-out. Notably, even when some HVR spikes persist through the spatial median filtering step, the adjacent NVRs typically remain prominent and exhibit a spatio-temporal pattern that is clearly distinct from those associated with avalanches. This characteristic provides an additional criterion for confirming traffic-related signals.

https://doi.org/10.5194/egusphere-2026-2373
Preprint. Discussion started: 5 June 2026

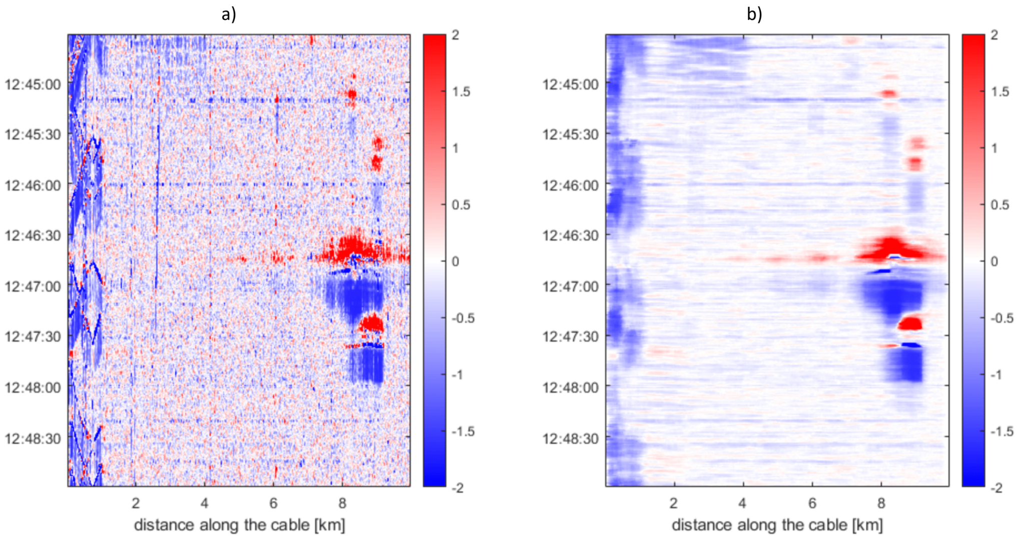

Figure 9. a) Raw attribute $\sigma_{\mathrm{tmp}}(t)$ and b) its spatially smoothed version $\sigma_{\mathrm{trig}}(t)$, for the avalanche signal shown in Fig. 5. Note the pronounced HVR patch in red, followed in time by a NVR patch, a pattern that distinguishes avalanche signals from most anthropogenic activities and noises.

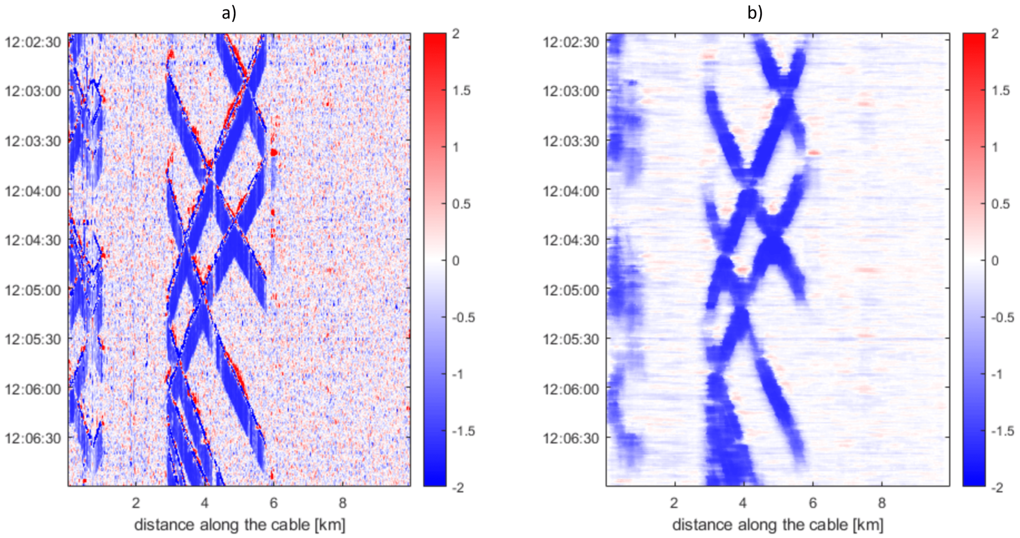

Figure 10. a) Raw attribute $\sigma_{\mathrm{tmp}}(t)$ and b) its spatially smoothed version $\sigma_{\mathrm{trig}}(t)$, for the traffic signal shown in Fig. 6.

3.3 Real-time feature analysis and detection

The core of our proposed approach lies in the real-time analysis of the $\sigma_{\text{trig}}(t,\forall x)$ attribute, leveraging the observation that avalanches and traffic events exhibit distinct, recognizable signatures in this domain. In practice, this involves continuously computing σ_{trig} and generating dynamic, real-time visualizations of the metric for initial triggering based on user-defined thresholds. Specifically, waterfall plots of σ_{trig} over the most recent T seconds of recorded data are analyzed in real time. The first step consists of detecting HVR spikes indicative of potential avalanche activity. This can be achieved with minimal latency exploiting the causal nature of the STA/LTA method. This initial detection then triggers subsequent analysis to assess whether a significant NVR region (hereafter referred to as NVR_1) is spatially adjacent to the detected HVR. Such adjacency indicates pronounced move-out and, therefore, suggests that the event is likely caused by a source along the cable, such as passing vehicles. A third diagnostic element is then extracted: another NVR (refereed to as NVR_2) that *temporally* (not spatially) follows the HVR triggering patch, potentially reflecting the low-frequency content generated by large avalanches. Although the triggering mechanism itself (i.e. HVR detection where $\sigma_{\text{trig}} > \sigma_{\text{threshold}}$) operates quasi-instantaneously, we recommend waiting at least 5 seconds before evaluating the spatially adjacent NVR_1 to allow for temporal development of the event, thereby introducing latency in the validation step, as opposed to the triggering. Naturally, determining the full spatio-temporal extent of the NVR_2 region requires the event to have concluded, which can potentially take several minutes.

Following the quasi-instantaneous event triggering phase, the proposed avalanche detection algorithm essentially becomes a pattern recognition task. Various approaches could be envisaged, including computer vision methods or AI-based classification techniques. In this work, we have adopted a simple yet efficient image-processing strategy. Specifically, connected-component analysis is applied to the σ_{trig} image domain to delineate contiguous regions of interest (HVR and NVR), after which region attributes are extracted to characterize their spatio-temporal extent. This approach is standard in image analysis (Rosenfeld and Pfaltz, 1966; Gonzalez and Woods, 2018) and can be implemented in widely used software libraries (e.g., bwconncomp and regionprops in MATLAB, or scipy.ndimage.label and skimage.measure.regionprops in Python).

4 Event Detection Results

This section presents and analyzes the performance of our avalanche detection algorithm using short-term average (STA) and long-term average (LTA) windows of 4 and 40 s, respectively. The low-frequency data were obtained using convolution with a Chebyshev operator achieving 80 dB attenuation at 5 Hz. The spatial median filter step (Eq. 3) was performed over a 360 m aperture. HVRs were identified as connected components with $\sigma_{\text{trig}} > 2$, while associated NVRs were searched using $\sigma_{\text{trig}} < -0.5$. The full acquisition period (131 days) was processed, therefore including both open (23 days) and closed (108 days) phases of the mountain road pass.

The quasi-instantaneous HVR detection resulted in a total of 2,643 triggers (704 during the road-closure period and 1939 during road-opening period) using a detection threshold $\sigma_{\text{trig}} = 2$. Fig.11 shows their distribution in time and space, with a

https://doi.org/10.5194/egusphere-2026-2373
Preprint. Discussion started: 5 June 2026

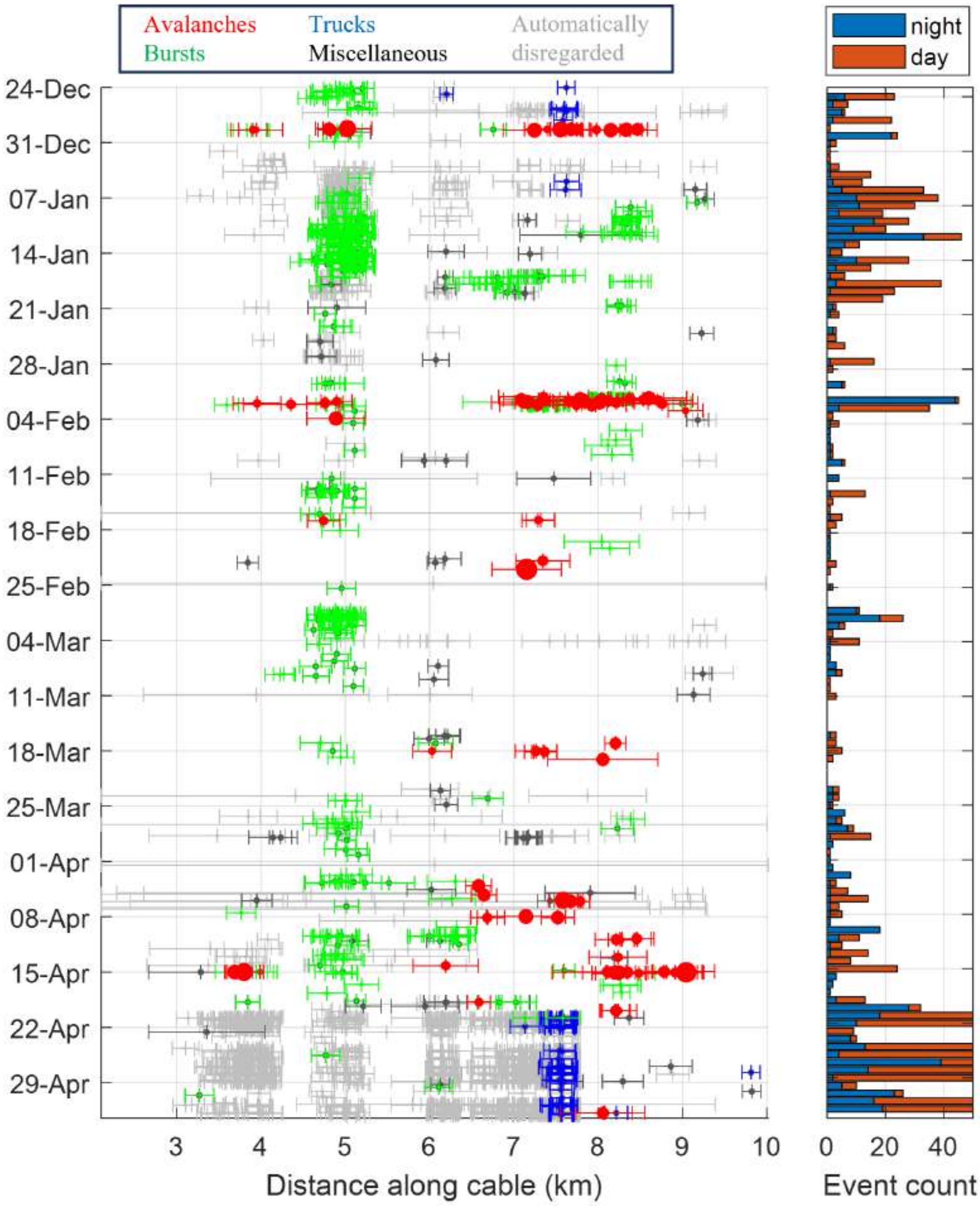

Figure 11. Results of the detection process applied over the whole acquisition period. Avalanches are shown in red, with point sizes corresponding to approximate event duration (time lag between HVR and NVR_2 onsets). Bursts events are displayed in green. Detected trucks without spatially adjacent NVR_1 (i.e. false positives) are in blue. Miscellaneous events (earthquakes, helicopters, snow clearance activity, etc) without an associated NVR_1 are displayed in black. All the other events with an associated NVR_1 are in light gray (mostly traffic). The number of events detected per day is shown on the right hand side panel. The event's spatial extents (displayed as error bars) correspond to the widths of the HVR (very large ones being earthquakes).

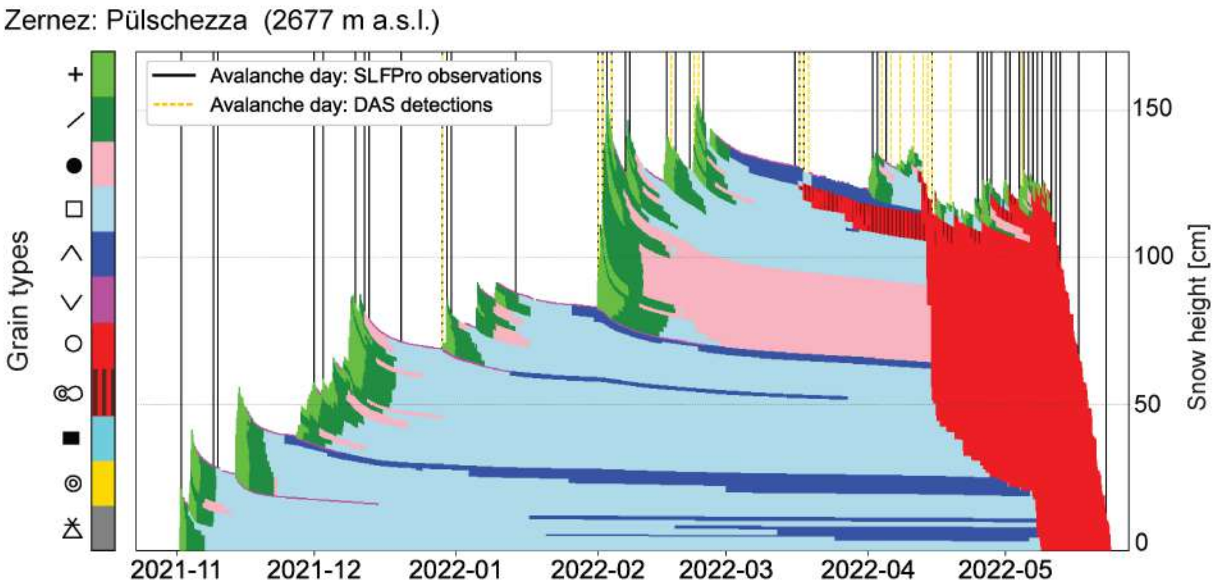

Figure 12. SNOWPACK simulation driven by data from the automatic weather stations located above Val Pülschezza in Zernez at 2677 m a.s.l. (situated approximately 6 km away from the typical avalanche release zones along the Flüelapass road). This shows the seasonal evolution of snow stratigraphy (colors and grain type labels follow the international snow classification; (Fierz et al.). The vertical lines indicate avalanche days reported in the SLFPro database (black) as well as detections with the DAS system (yellow).

breakdown by day and night. While the trigger count may appear excessive at first glance, note that a single physical event can produce multiple closely-spaced HVR patches, as illustrated in Figures B1–B7.

Another important aspect putting the total trigger count into perspective is the cumulative spatio-temporal extent of the HVRs, which represents 0.3 ‰ of the dataset over the open-pass period, and only 0.03 ‰ during the closed-pass period. Neglecting the spatial extent and considering exclusively the time during which any part of the cable experiences HVR activity, the cumulative triggering duration amounts to less than 1 hour during the whole road-closure period (0.36 ‰ of 108 days) and only 2.5 hours during the road-opening phase (4.5 ‰ of 23 days). The latter represents a negligible proportion compared to what a conventional STA/LTA approach would yield, likely triggering quasi-continuously along the road during daytime.

Manual visualization becomes achievable after such substantial data volume reduction, and all triggering windows were manually clustered based on the overall signal morphology in both the ϵ and σ domains, i.e., looking at large enough spatio-temporal windows to identify and track potential vehicle traffic moveout. We chose to group triggers into four principal categories: avalanches, bursts, traffic, and miscellaneous signals such as earthquakes, helicopters, or other localized activity.

The largest cluster (1688 occurrences) is traffic-related, in particular after April 21st when the pass reopened in spring. In contrast to the pass-closure period that exhibits a median count of just 3 triggers per day, the daily trigger counts during the road-opening period frequently exceeded 200 (note that the axis in Fig. 11 is clipped at 50), with a clear concentration during daylight hours. Interestingly, weekend counts (e.g., April 24th and 30th, both Saturdays) were lower despite higher recreational traffic volumes, suggesting that weekday work-related traffic, i.e. trucks, is the dominant source of initial triggers. Visual inspection confirmed that around 94% of vehicle related triggers were induced by trucks rather than cars. As shown in Figure B5, unlike cars, trucks produce significantly higher-amplitude signals that remain visible beyond 6 km distance (i.e., where the cable diverges from the road). From the perspective of a purely HVR-based detector, truck generated signals can easily be misinterpreted as avalanches, but our proposed move-out identification strategy substantially mitigates this issue. Assessing whether an NVR region is spatially adjacent to the HVR patch enabled the automatic rejection of 66% of truck-induced triggers (shown in gray in Fig. 11). The remaining false positives (in blue) are concentrated around 7.5 km distance, and are likely due to a road surface irregularity that generates noise resembling avalanche signatures. A drastic mitigation would be to exclude this section of the cable, but this approach would obviously result in missing genuine avalanche events at that location. Alternatively, truck trajectories could be tracked from signals observed between 4–6 km, but this would require analyzing large spatio-temporal windows and the robust implementation of a fully automated tracking strategy seems challenging.

Another significant source of initial triggers consists of short impulsive transient events (459 occurrences), hereafter referred to as “bursts”, to which the algorithm is particularly sensitive. These are marked in green in Figure 11. They occur most frequently around the 5 km distance, corresponding to a relatively flat topographic section where the riverbank widens. The precise nature of these bursts remains under investigation. Some appear completely isolated, such as the event at 100 s and 5 km in Fig. B1, a time window also containing three easily recognizable avalanches. Many bursts can also be observed following snow mass activity, like in Fig. B2, which shows a prominent avalanche followed by at least nine bursts, each triggering within the 10-minute window. They are not shown in the figure, but numerous additional similar sub-events followed in the subsequent hour, contributing to the high trigger count in the night of February 1st. These bursts may reflect structural reconfigurations of the snowpack, in particular post-avalanche. Importantly, their short duration (typically around 5 s) helps to distinguish them from snow avalanches. Most of the remaining triggers fall into the miscellaneous category including earthquakes, helicopters, or other activities, some of which could be related to snow clearance.

Finally, we identified 82 triggers exhibiting a localized σ response consistent with snow avalanche activity. These correspond to 73 potential avalanche events, two of which occurred after the pass was reopened. All candidate events are shown in red in Fig. 11, highlighting three major avalanche episodes: around January 29th, February 1st, and April 15th. Although we cannot unequivocally confirm that all identified events correspond to true avalanches (some are barely distinguishable in the raw strain-rate data) they all exhibit a plausible σ signature. Among them, 20 events are unambiguous, leaving little room for doubt, particularly those independently confirmed by field observations on March 19th (Fig. 3) and April 15th (Figs. 4 and 5). The timing of these avalanche detections is also consistent with avalanche observations in the area (black lines in Fig. 12) and is further supported by the meteorological conditions and snow cover characteristics (see Section A for a detailed description). For example, avalanches detected on January 29th coincide with the onset of a snowfall episode over a weakly bonded snow cover containing persistent weak layers in the snowpack that are commonly associated with avalanching (Section A). In the following days, during a storm, numerous avalanches were also detected by the DAS system and reported in SLFPro (Fig. 12), while new snow accumulations reached 80 cm at high elevations (Fig. A1a). Three additional snowfall events in February also coincided with avalanches detected by DAS or reported in SLFPro observations. From mid-March onward, the snowpack became progressively wetter, reaching fully wet snow cover conditions by April 12th at the elevation of the Zernez weather station (Fig. A1a). This transition occurred earlier at lower elevations (Fig. A1b) and on south-facing slopes. During this period, several wet-snow avalanches were detected by DAS, some of which were visually confirmed by camera images, and others were reported in SLFPro.

In summary, these results demonstrate that the proposed method can rapidly identify potential avalanche activity while remaining largely robust to traffic, the dominant anthropogenic noise source. This represents a key achievement of the approach. Nevertheless, a non-negligible number of false triggers persist. Although characteristic features such as duration, spatial extent, signal energy, or peak amplitude could, in principle, provide additional discrimination, no single set of deterministic features was identified that can automatically eliminate false alerts without risking the omission of genuine avalanche events. The primary challenge lies in the robust extraction of spatio-temporal attributes, which is hindered by the complexity and variability of signal morphologies. Avalanche signatures themselves exhibit substantial diversity in spectral content, spatial extent, duration, and potential secondary transient activity, thereby limiting the effectiveness of simple rule-based discriminators. This suggests that more advanced signal characterization strategies are required to improve automated classification performance. Another avenue could consist of incorporating contextual information. Variables such as snowpack stability indices and meteorological conditions (e.g., recent precipitation and temperature evolution) provide valuable prior information regarding avalanche likelihood and anthropogenic activity levels. Integrating such external data streams could enable adaptive thresholding or probabilistic decision frameworks that dynamically adjust the system sensitivity both spatially and temporally according to environmental conditions. In this context, machine learning approaches offer a particularly promising perspective, not only for enhanced signal characterization, but also for the integration of heterogeneous data sources and the learning of context-dependent decisions. Such developments could ultimately reduce false alerts while preserving high sensitivity to genuine avalanche events.

5 Conclusions

This study demonstrates that DAS using existing telecommunication cables can be a viable and cost-effective method for large-scale detection of snow avalanches in near real-time. Crucially, our findings show that avalanches, some of which do not physically reach the cable, can be identified based on their seismo-acoustic signatures, as verified through photographic evidence.

We introduced a new spatio-temporal detection attribute, σ_{trig}, derived from dual-frequency STA/LTA analysis, which enabled discrimination of avalanche activity from the most common vehicle traffic activity, with near-field signal generated by cars very rarely triggering. Truck-induced signals are more challenging to discriminate; however, most can be identified based on their slow move-out, which is emphasized by a spatially adjacent NVR signature. Our detection workflow triggered only 4.5 ‰ of the time when the pass was open to traffic, and only 0.36 ‰ of the time when closed, enabling the identification of 73 potential avalanches without manual oversight except for validation.

The algorithm is efficient and robust against ambient noise, therefore scalable across long cable segments. In contrast to black-box AI models, our proposed approach is based on basic signal and image processing, therefore ensuring interpretability and ease of implementation. Nonetheless, looking ahead, we envision a hybrid detection framework that integrates our physics-informed metric with the advanced pattern recognition capabilities of machine learning techniques. Moreover, integrating contextual information such as meteorological conditions or snowpack stability indices should enable more robust detection by adaptive spatio-temporal thresholding and probabilistic decision making to reduce false alerts while preserving sensitivity. Overall, this work provides a foundation for the operational use of DAS in real-time natural hazard monitoring and, more broadly, for the detection of gravity-driven natural hazards in remote environments.

Code and data availability. The Matlab scripts used to reproduce the detection workflow and the appendix demonstration figures, together with representative DAS data excerpts, are publicly available on Zenodo (DOI: 10.5281/zenodo.20347445). The full DAS dataset generated during the monitoring campaign is not publicly available due to its size and restrictions related to the underlying telecommunication infrastructure.

Appendix A: SNOWPACK simulations

The two automatic weather stations used in this study are located in Zernez (Val Pülschezza, 2677 m a.s.l.) and Davos (Stilli, 1563 m a.s.l.) and belong to the Intercantonal Measurement and Information System (IMIS) network (https://www.envidat.ch/#/metadata/imis-measuring-network). This large-scale network of automatic weather stations is distributed across the Swiss Alps in high-alpine terrain. The stations measure snow height, air and snow surface temperatures, wind speed and direction, relative humidity, incoming shortwave radiation, and precipitation in real time. Based on these measurements, snow-cover simulations are automatically computed for each station during the winter season using the one-dimensional, physically based, multi-layer SNOWPACK model (Lehning et al., 2002; Bartelt and Lehning, 2002). These data and simulations are used operationally by the Swiss avalanche warning service to assess avalanche hazard daily (Morin et al., 2020). Among several parameters, the SNOWPACK model outputs the seasonal snow stratigraphy together with the dominant grain type in each simulated layer (upper simulations in Fig. A1). These grain types illustrate how snowfall, snow metamorphism, and melt processes control the temporal and vertical evolution of the simulated snow layers. For instance, snowfall episodes are associated with new snow layers, represented by green grain types in the SNOWPACK simulations shown in Fig. A1. Blue layers correspond to persistent weak layers in the snowpack, such as faceted crystals or depth hoar. The presence of new snow overlying a poorly bonded persistent weak layer is a common condition for the release of natural dry-snow avalanches (Schweizer et al., 2003). In contrast, wet-snow avalanche release is primarily driven by the infiltration of liquid water into the snowpack (Mitterer and Schweizer, 2013). This process is represented by the liquid water content, another parameter provided by the SNOWPACK model (lower simulations in Fig. A1). Based on this parameter, the snowpack can be classified as dry when the liquid water content is 0%, moist when $< 3\%$, and wet when $\geq 3\%$ (Techel, 2010).

https://doi.org/10.5194/egusphere-2026-2373
Preprint. Discussion started: 5 June 2026

a) Zernez: Pülschezza (2677 m a.s.l.)

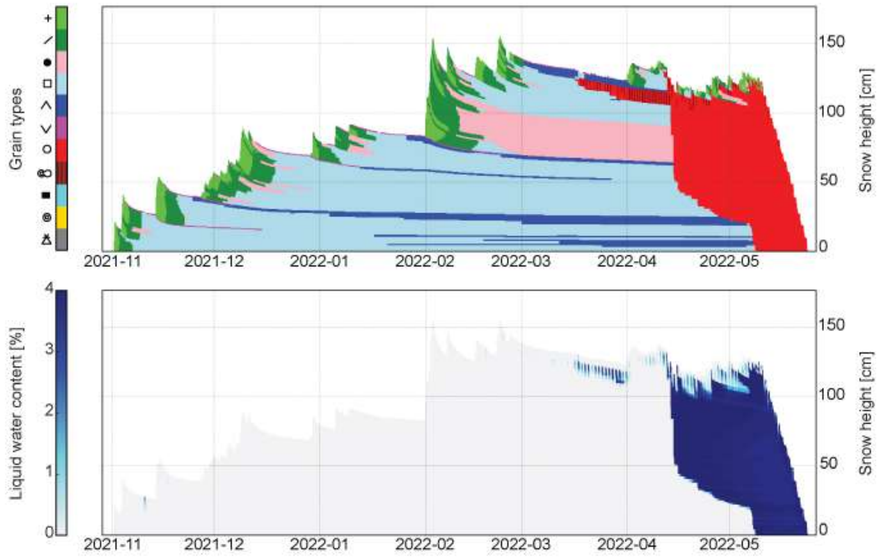

b) Davos: Stilli (1563 m a.s.l.)

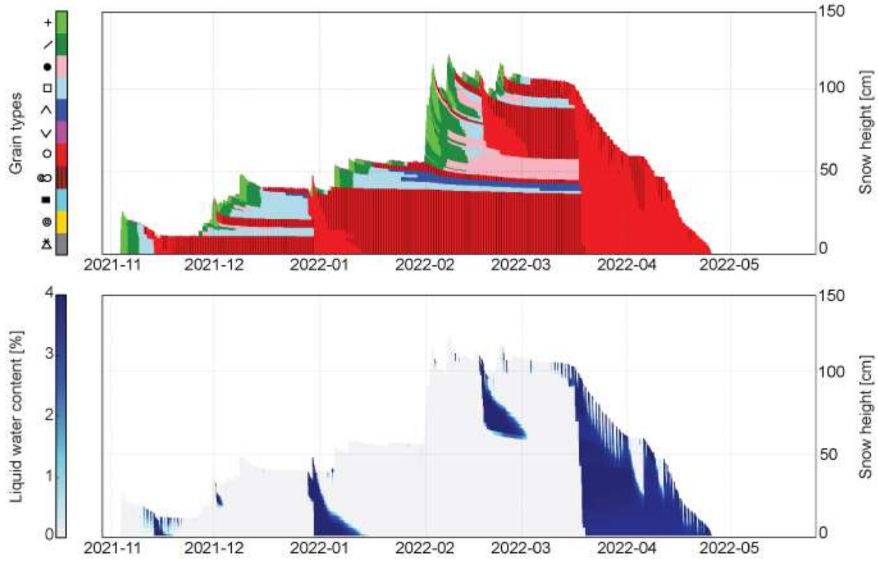

Figure A1. SNOWPACK simulations driven with data from the automatic weather stations located a) above Val Pülschezza in Zernez at 2677 m a.s.l., between 5 and 7 km from the typical avalanche release zones along the Flüelapass road, and b) Stilli in Davos at the start of the Flüelapass road at 1563 m a.s.l. The upper simulations show the seasonal evolution of snow stratigraphy (colors and grain type labels follow the international snow classification; (Fierz et al.)), and the lower simulations show the liquid water content in percentage. The vertical axis shows the evolution of snow height over time.

360 ## Appendix B: Further data examples

The figures below illustrate the variety of events with their spatio-temporal σ_{trig} responses.

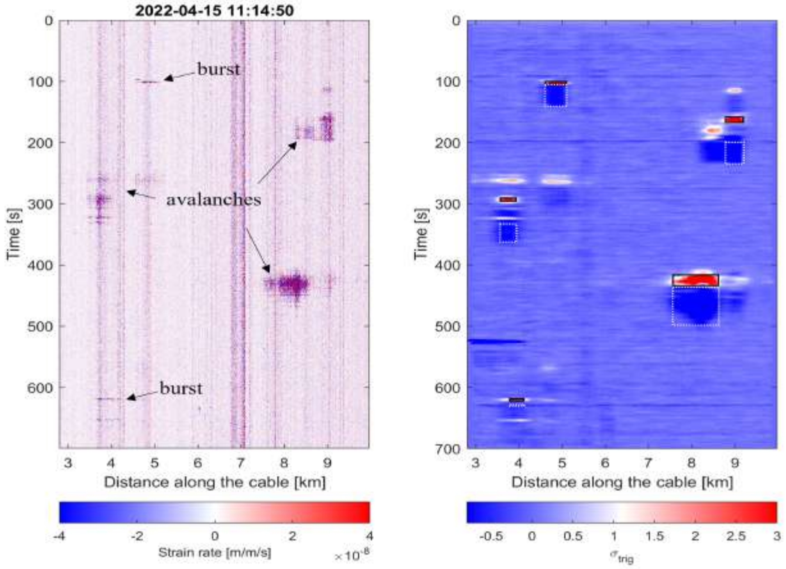

Figure B1. Avalanche window example. HVR patches ($\sigma_{trig} > 2$, black rectangles) are automatically detected with minimal latency. Two bursts are also detected. The dashed white rectangle shows NVR_2. Note the absence of spatially adjacent NVR_1 patches here (shown in green in subsequent figures).

https://doi.org/10.5194/egusphere-2026-2373
Preprint. Discussion started: 5 June 2026

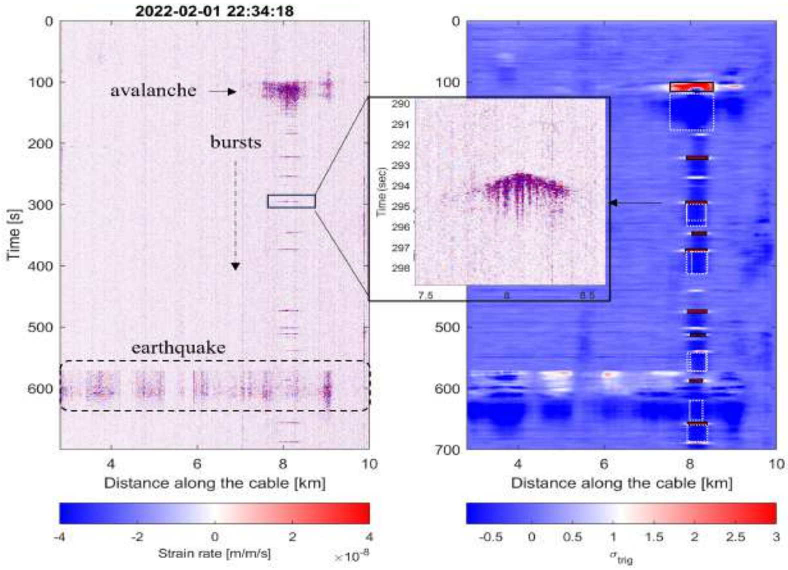

Figure B2. Avalanche example, resulting in several triggers due to follow up bursts explaining the high event count of February 1st in Fig. 11b. An earthquake is also visible, but did not trigger.

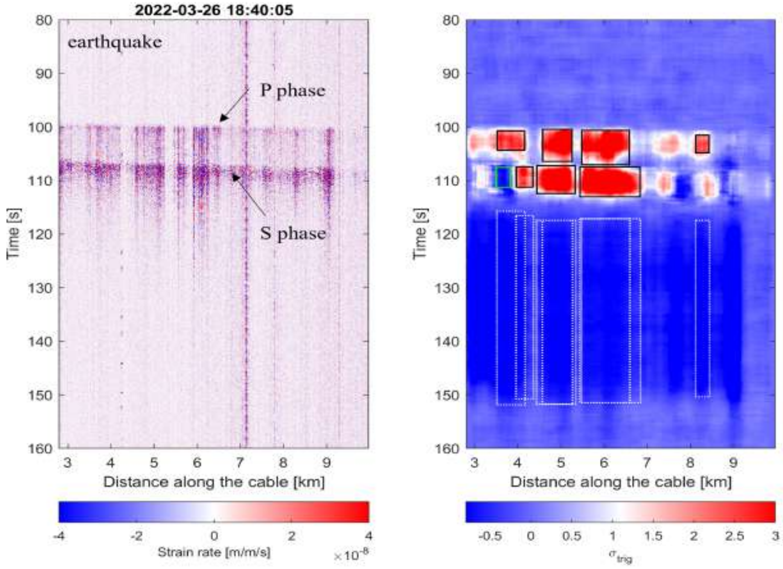

Figure B3. Earthquake example, resulting in multiple HVR triggers.

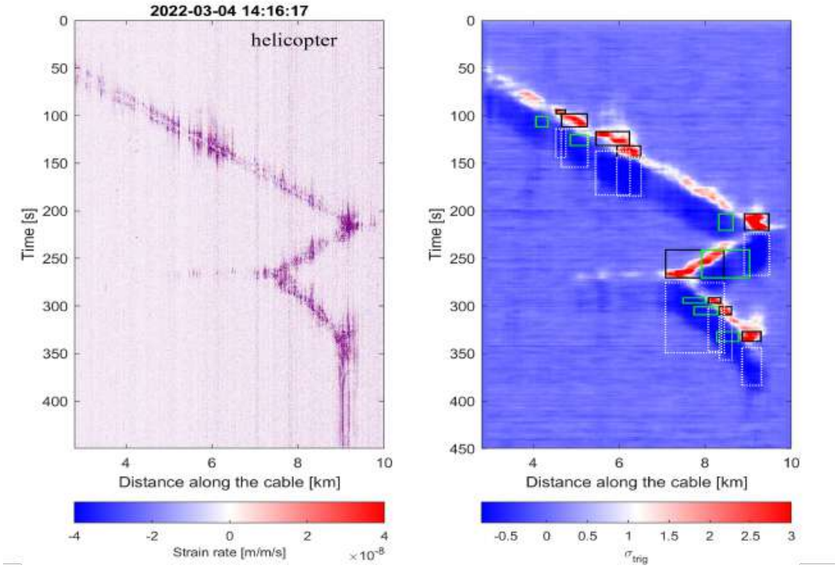

Figure B4. Helicopter signal example, resulting in multiple triggers (all of them invalidated based on the subsequent detection of an associated spatially adjacent NVR$_1$ in green).

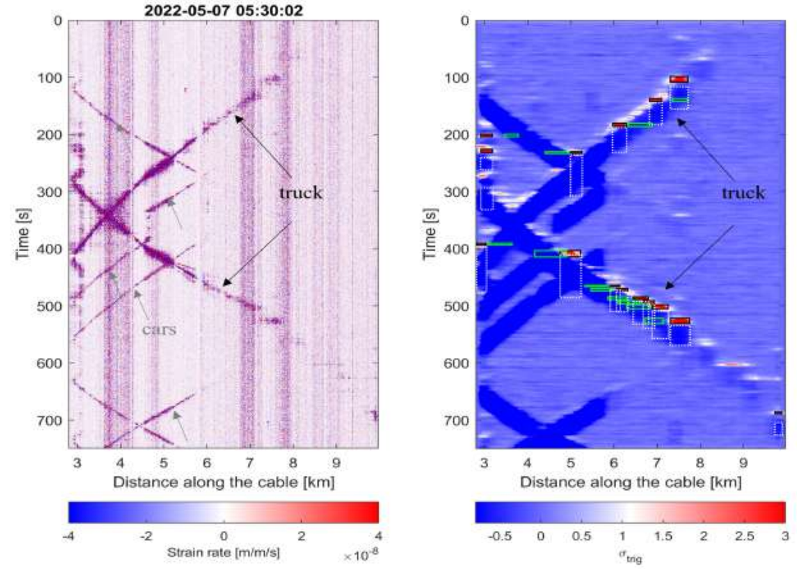

Figure B5. Traffic example. The car signals (black arrows) vanishe after 6 km distance, in contrast to trucks which generate multiple triggers (most of them invalidated based on the subsequent detection of an associated spatially adjacent NVR$_1$ in green).

https://doi.org/10.5194/egusphere-2026-2373
Preprint. Discussion started: 5 June 2026

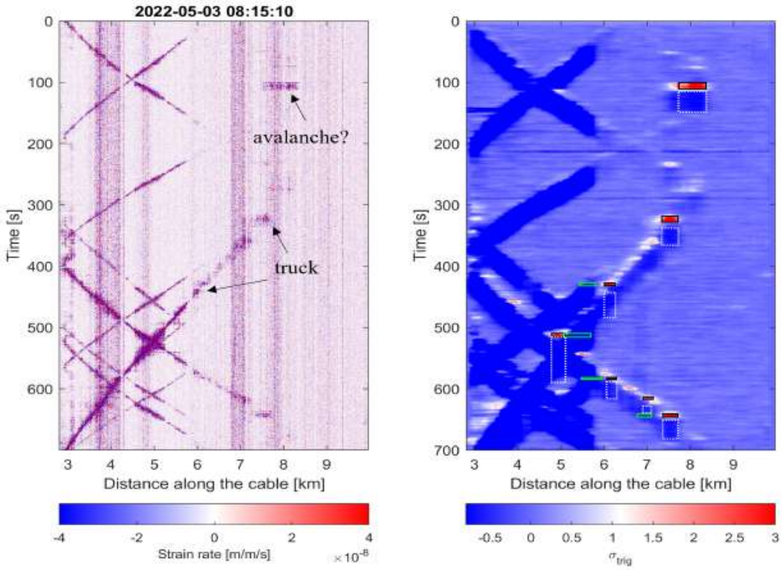

Figure B6. Another traffic example, further demonstrating the robustness of the process against car generated signals (distances < 6 km), while trucks are more challenging to discriminate, especially at ~ 7.5 km distance.

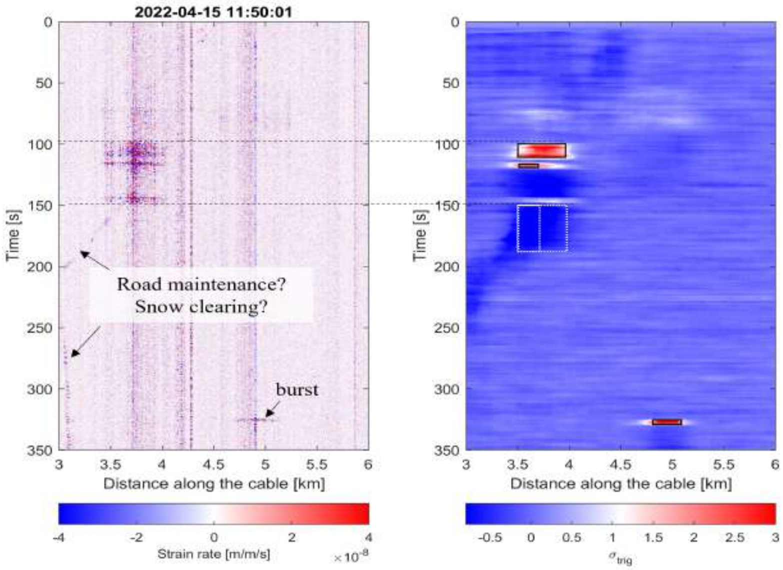

Figure B7. Avalanche example potentially triggered by human activity. The time delay between HVR (black rectangle) and NVR$_2$ (dashed white rectangle) is generally, but not systematically, a good proxy to the avalanche duration.

Author contributions. FW, AF, PE and PP conceived the project. PE and PP conducted the experiment. PE and AF supervised the project. PE developed the algorithm and performed the analysis. JA, CPG, AS and AvH contributed in methodology refinements and to the interpretation of results. All authors contributed to the manuscript redaction, and approved the present version.

Competing interests. The contact author has declared that none of the authors has any competing interests.

Acknowledgements. We gratefully acknowledge the support by Swisscom in the form of free access to the telecommunication cable along the Flüelapass road. We also thank Lars Gebraad for the drone footage. This work was supported by the Swiss National Science Foundation (SNSF) under Grant No. 10001041.

References

Allen, R. V.: Automatic earthquake recognition and timing from single traces, Bulletin of the Seismological Society of America, 68, 1521–1532, https://doi.org/https://doi.org/10.1785/BSSA0680051521, 1978.

Allstadt, K. E., Matoza, R. S., Lockhart, A. B., Moran, S. C., Caplan-Auerbach, J., Haney, M. M., Thelen, W. A., and Malone, S. D.: Seismic and acoustic signatures of surficial mass movements at volcanoes, Journal of Volcanology and Geothermal Research, 364, 76–106, https://doi.org/https://doi.org/10.1016/j.jvolgeores.2018.09.007, 2018.

Badoux, A., Andres, N., Techel, F., and Hegg, C.: Natural hazard fatalities in Switzerland from 1946 to 2015, Natural Hazards and Earth System Sciences, 16, 2747–2768, https://doi.org/https://doi.org/10.5194/nhess-16-2747-2016, 2016.

Barla, M., Aiassa, S., Antolini, F., Insana, A., Gaudino, R., Rizzelli Martella, G., and Pellegrini, S.: A New Real-Time Debris Flow and Snow Avalanche Detection System Based on Optical Fiber Sensing, Landslides, 22, 1367–1382, https://doi.org/https://doi.org/10.1007/s10346-024-02399-2, 2025.

Baroudi, D., Sovilla, B., and Thibert, E.: Effects of Flow Regime and Sensor Geometry on Snow Avalanche Impact-Pressure Measurements, Journal of Glaciology, 57, 277–288, https://doi.org/https://doi.org/10.3189/002214311796405988, 2011.

Bartelt, P. and Lehning, M.: A physical SNOWPACK model for the Swiss avalanche warning: Part I: numerical model, Cold Regions Science and Technology, 35, 123–145, https://doi.org/https://doi.org/10.1016/S0165-232X(02)00074-5, 2002.

Booth, A., Christoffersen, P., Pretorius, A., Chapman, J., Smith, E., Ridder, S., Nowacki, A., Lipovsky, B., and Denolle, M.: Characterising sediment thickness beneath a Greenlandic outlet glacier using distributed acoustic sensing: preliminary observations and progress towards an efficient machine learning approach, Annals of Glaciology, 63, 79–82, https://doi.org/https://doi.org/10.1017/aog.2023.15, 2023.

Booth, A. D., Christoffersen, P., Schoonman, C., Clarke, A., Hubbard, B., Law, R., Doyle, S. H., Chudley, T. R., and Chalari, A.: Distributed Acoustic Sensing of Seismic Properties in a Borehole Drilled on a Fast-Flowing Greenlandic Outlet Glacier, Geophysical Research Letters, 47, https://doi.org/https://doi.org/10.1029/2020GL088148, 2020.

Brisbourne, A. M., Kendall, M., Kufner, S.-K., Hudson, T. S., and Smith, A. M.: Downhole distributed acoustic seismic profiling at Skytrain Ice Rise, West Antarctica, The Cryosphere, 15, 3443–3458, https://doi.org/https://doi.org/10.5194/tc-15-3443-2021, 2021.

Bründl, M., Etter, H.-J., Steiniger, M., Klingler, C., Rhyner, J., and Ammann, W. J.: IFKIS - a basis for managing avalanche risk in settlements and on roads in Switzerland, Natural Hazards and Earth System Sciences, 4, 257–262, https://doi.org/https://doi.org/10.5194/nhess-4-257-2004, 2004.

Caduff, R., Wiesmann, A., Bühler, Y., and Pielmeier, C.: Continuous Monitoring of Snowpack Displacement at High Spatial and Temporal Resolution with Terrestrial Radar Interferometry, Geophysical Research Letters, 42, 813–820, https://doi.org/https://doi.org/10.1002/2014GL062442, 2015.

Chiarle, M., Geertsema, M., Mortara, G., and Clague, J. J.: Relations between climate change and mass movement: Perspectives from the Canadian Cordillera and the European Alps, Global and Planetary Change, 202, 103 499, https://doi.org/https://doi.org/10.1016/j.gloplacha.2021.103499, 2021.

Chmiel, M., Walter, F., Wenner, M., Zhang, Z., McArdell, B. W., and Hibert, C.: Machine Learning Improves Debris Flow Warning, Geophysical Research Letters, 48, https://doi.org/https://doi.org/10.1029/2020GL090874, 2021.

Denissova, N., Nurakynov, S., Petrova, O., Chepashev, D., Daumova, G., and Yelisseyeva, A.: Remote Sensing Techniques for Assessing Snow Avalanche Formation Factors and Building Hazard Monitoring Systems, Atmosphere, 15, https://doi.org/https://doi.org/10.3390/atmos15111343, 2024.

Dietze, M., Mohadjer, S., Turowski, J. M., Ehlers, T. A., and Hovius, N.: Seismic monitoring of small alpine rockfalls – validity, precision and limitations, Earth Surface Dynamics, 5, 653–668, https://doi.org/https://doi.org/10.5194/esurf-5-653-2017, 2017.

Dilley, M.: Natural disaster hotspots: a global risk analysis, vol. 5, World Bank Publications, http://documents.worldbank.org/curated/en/621711468175150317, 2005.

Eckerstorfer, M., Bühler, Y., Frauenfelder, R., and Malnes, E.: Remote sensing of snow avalanches: Recent advances, potential, and limitations, Cold Regions Science and Technology, 121, 126–140, https://doi.org/https://doi.org/10.1016/j.coldregions.2015.11.001, 2016.

Eckert, N., Corona, C., Giacona, F., Gaume, J., Mayer, S., van Herwijnen, A., Hagenmuller, P., and Stoffel, M.: Climate change impacts on snow avalanche activity and related risks, Nature Reviews Earth and Environment, 5, 369–389, https://doi.org/https://doi.org/10.1038/s43017-024-00540-2, 2024.

Emberson, R., Kirschbaum, D., and Stanley, T.: New global characterisation of landslide exposure, Natural Hazards and Earth System Sciences, 20, 3413–3424, https://doi.org/https://doi.org/10.5194/nhess-20-3413-2020, 2020.

Fichtner, A., Klaasen, S., Thrastarson, S., Çubuk-Sabuncu, Y., Paitz, P., and Jónsdóttir, K.: Fiber-Optic Observation of Volcanic Tremor through Floating Ice Sheet Resonance, The Seismic Record, 2, 148–155, https://doi.org/https://doi.org/10.1785/0320220010, 2022.

Fichtner, A., Hofstede, C., N. Kennett, B. L., Nymand, N. F., Lauritzen, M. L., Zigone, D., and Eisen, O.: Fiber-Optic Airplane Seismology on the Northeast Greenland Ice Stream, The Seismic Record, 3, 125–133, https://doi.org/https://doi.org/10.1785/0320230004, 2023.

Fichtner, A., Hofstede, C., Kennett, B. L. N., Svensson, A., Westhoff, J., Walter, F., Ampuero, J.-P., Cook, E., Zigone, D., Jansen, D., and Eisen, O.: Hidden cascades of seismic ice stream deformation, Science, 387, 858–864, https://doi.org/https://doi.org/10.1126/science.adp8094, 2025.

Fierz, C., Mcclung, D. M., Satyawali, P. K., and Sokratov, S. A.: The International classification for seasonal snow on the ground; Technical documents in Hydrology; Vol.:83; 2009.

Froude, M. J. and Petley, D. N.: Global fatal landslide occurrence from 2004 to 2016, Natural Hazards and Earth System Sciences, 18, 2161–2181, https://doi.org/https://doi.org/10.5194/nhess-18-2161-2018, 2018.

Fuchs, S., Thoeni, M., McAlpin, M., Gruber, U., and Bründl, M.: Avalanche Hazard Mitigation Strategies Assessed by Cost Effectiveness Analyses and Cost Benefit Analyses—evidence from Davos, Switzerland, Natural Hazards, 41, 113–129, https://doi.org/https://doi.org/10.1007/s11069-006-9031-z, 2007.

Gauer, P., Kern, M., Kristensen, K., Lied, K., Rammer, L., and Schreiber, H.: On pulsed Doppler radar measurements of avalanches and their implication to avalanche dynamics, Cold Regions Science and Technology, 50, 55–71, https://doi.org/https://doi.org/10.1016/j.coldregions.2007.03.009, snow and Avalanches EGU 2006, 2007.

Gonzalez, R. C. and Woods, R. E.: Digital Image Processing, Pearson, 4 edn., ISBN 978-0133356724, 2018.

Hammer, C., Fäh, D., and Ohrnberger, M.: Automatic detection of wet-snow avalanche seismic signals, Natural Hazards, 86, 601–618, https://doi.org/https://doi.org/10.1007/s11069-016-2707-0, 2017.

Hartog, A.: An Introduction to Distributed Optical Fibre Sensors, CRC press, ISBN 978-1482259575, https://doi.org/https://doi.org/10.1201/9781315119014, 2017.

Heck, M., Herwijnen, A. V., Hammer, C., Hobiger, M., Schweizer, J., and Fäh, D.: Automatic detection of avalanches combining array classification and localization, Earth Surface Dynamics, 7, 491–503, https://doi.org/https://doi.org/10.5194/esurf-7-491-2019, 2019a.

Heck, M., Hobiger, M., van Herwijnen, A., Schweizer, J., and Fäh, D.: Localization of seismic events produced by avalanches using multiple signal classification, Geophysical Journal International, 216, 201–217, https://doi.org/10.1093/gji/ggy394, 2019b.

Hudson, T. S., Baird, A. F., Kendall, J. M., Kufner, S. K., Brisbourne, A. M., Smith, A. M., Butcher, A., Chalari, A., and Clarke, A.: Distributed Acoustic Sensing (DAS) for Natural Microseismicity Studies: A Case Study From Antarctica, Journal of Geophysical Research: Solid Earth, 126, https://doi.org/https://doi.org/10.1029/2020JB021493, 2021.

Hürlimann, M., Coviello, V., Bel, C., Guo, X., Berti, M., Graf, C., Hübl, J., Miyata, S., Smith, J. B., and Yin, H.-Y.: Debris-flow monitoring and warning: Review and examples, Earth-Science Reviews, 199, 102 981, https://doi.org/https://doi.org/10.1016/j.earscirev.2019.102981, 2019.

Kang, J., Walter, F., Paitz, P., Aichele, J., Edme, P., Meier, L., and Fichtner, A.: Automatic Monitoring of Rock-Slope Failures Using Distributed Acoustic Sensing and Semi-Supervised Learning, Geophysical Research Letters, 51, https://doi.org/https://doi.org/10.1029/2024GL110672, 2024.

Klaasen, S., Paitz, P., Lindner, N., Dettmer, J., and Fichtner, A.: Distributed Acoustic Sensing in Volcano-Glacial Environments—Mount Meager, British Columbia, Journal of Geophysical Research: Solid Earth, 126, https://doi.org/https://doi.org/10.1029/2021JB022358, 2021.

Kleine, F., Bruland, C., Wuestefeld, A., Oye, V., and Landrø, M.: Seismic signal characterization of snow avalanches using distributed acoustic sensing in Grasdalen, western Norway, Natural Hazards and Earth System Sciences, 25, 2771–2782, https://doi.org/https://doi.org/10.5194/nhess-25-2771-2025, 2025.

Köhler, A., McElwaine, J. N., Sovilla, B., Ash, M., and Brennan, P.: The Dynamics of Surges in the 3 February 2015 Avalanches in Vallée de La Sionne, Journal of Geophysical Research: Earth Surface, 121, 2192–2210, https://doi.org/https://doi.org/10.1002/2016JF003887, 2016.

Köhler, A., McElwaine, J. N., and Sovilla, B.: GEODAR Data and the Flow Regimes of Snow Avalanches, Journal of Geophysical Research: Earth Surface, 123, 1272–1294, https://doi.org/https://doi.org/10.1002/2017JF004375, 2018.

Köhler, A., Lok, L. B., Felbermayr, S., Peters, N., Brennan, P. V., and Fischer, J.-T.: mGEODAR—A Mobile Radar System for Detection and Monitoring of Gravitational Mass-Movements, Sensors, 20, https://doi.org/https://doi.org/10.3390/s20216373, 2020.

Lacroix, P. and Helmstetter, A.: Location of Seismic Signals Associated with Microearthquakes and Rockfalls on the Séchilienne Landslide, French Alps, Bulletin of the Seismological Society of America, 101, 341–353, https://doi.org/https://doi.org/10.1785/0120100110, 2011.

Lacroix, P., Grasso, J.-R., Roulle, J., Giraud, G., Goetz, D., Morin, S., and Helmstetter, A.: Monitoring of snow avalanches using a seismic array: Location, speed estimation, and relationships to meteorological variables, Journal of Geophysical Research: Earth Surface, 117, https://doi.org/https://doi.org/10.1029/2011JF002106, 2012.

Lawrence, W. F. S. and Williams, T. R.: Seismic Signals Associated with Avalanches, Journal of Glaciology, 17, 521 – 526, https://doi.org/https://doi.org/10.3189/S0022143000013782, 1976.

Lehning, M., Bartelt, P., Brown, B., Fierz, C., and Satyawali, P.: A physical SNOWPACK model for the Swiss avalanche warning: Part II. Snow microstructure, Cold Reg. Sci. Technol., 35, 147–167, https://doi.org/10.1016/S0165-232X(02)00073-3, 2002.

Lindsey, N. J. and Martin, E. R.: Fiber-optic seismology, Annual Review of Earth and Planetary Sciences, 49, 309–336, https://doi.org/https://doi.org/10.1146/annurev-earth-072420-065213, 2021.

Lindsey, N. J., Rademacher, H., and Ajo-Franklin, J. B.: On the Broadband Instrument Response of Fiber-Optic DAS Arrays, Journal of Geophysical Research: Solid Earth, 125, e2019JB018 145, https://doi.org/https://doi.org/10.1029/2019JB018145, 2020.

Marchetti, E., Ripepe, M., Ulivieri, G., and Kogelnig, A.: Infrasound array criteria for automatic detection and front velocity estimation of snow avalanches: towards a real-time early-warning system, Natural Hazards and Earth System Sciences, 15, 2545–2555, https://doi.org/https://doi.org/10.5194/nhess-15-2545-2015, 2015.

Mayer, S., van Herwijnen, A., Ulivieri, G., and Schweizer, J.: Evaluating the performance of an operational infrasound avalanche detection system at three locations in the Swiss Alps during two winter seasons, Cold Regions Science and Technology, 173, 102 962, https://doi.org/https://doi.org/10.1016/j.coldregions.2019.102962, 2020.

Meier, L., Jacquemart, M., Blattmann, B., and Arnold, B.: Real-Time Avalanche Detection with Long-Range, Wide-Angle Radars for Road Safety in Zermatt, Switzerland, in: Proc. International Snow Science Workshop, pp. 304–308, https://www.geopraevent.ch/wp-content/uploads/2016/10/Avalanche-detection_Dr.-Lorenz-Meier_ISSW2016.pdf, 2016.

Mitterer, C. and Schweizer, J.: Analysis of the snow-atmosphere energy balance during wet-snow instabilities and implications for avalanche prediction, The Cryosphere, 7, 205–216, https://doi.org/https://doi.org/10.5194/tc-7-205-2013, 2013.

Morin, S., Horton, S., Techel, F., Bavay, M., Coléou, C., Fierz, C., Gobiet, A., Hagenmuller, P., Lafaysse, M., Ližar, M., et al.: Application of physical snowpack models in support of operational avalanche hazard forecasting: A status report on current implementations and prospects for the future, Cold Reg. Sci. Technol., 170, 102 910, https://doi.org/https://doi.org/10.1016/j.coldregions.2019.102910, 2020.

Paitz, P., Edme, P., Gräff, D., Walter, F., Doetsch, J., Chalari, A., Schmelzbach, C., and Fichtner, A.: Empirical Investigations of the Instrument Response for Distributed Acoustic Sensing (DAS) across 17 Octaves, Bulletin of the Seismological Society of America, 111, 1–10, https://doi.org/https://doi.org/10.1785/0120200185, 2020.

Paitz, P., Lindner, N., Edme, P., Huguenin, P., Hohl, M., Sovilla, B., Walter, F., and Fichtner, A.: Phenomenology of Avalanche Recordings From Distributed Acoustic Sensing, Journal of Geophysical Research: Earth Surface, 128, e2022JF007 011, https://doi.org/https://doi.org/10.1029/2022JF007011, 2023.

Petley, D.: Global patterns of loss of life from landslides, Geology, 40, 927–930, https://doi.org/https://doi.org/10.1130/G33217.1, 2012.

Prokop, A., Schön, P., Wirbel, A., and Jungmayr, M.: Monitoring avalanche activity using distributed acoustic fiber optic sensing, in: Proceedings of the international snow science workshop, pp. 129–133, https://arc.lib.montana.edu/snow-science/item/2040, 2014.

Pérez- Guillén, C., Sovilla, B., Suriñach, E., Tapia, M., and Köhler, A.: Deducing avalanche size and flow regimes from seismic measurements, Cold Regions Science and Technology, 121, 25–41, https://doi.org/https://doi.org/10.1016/j.coldregions.2015.10.004, 2016.

Pérez-Guillén, C., Tsunematsu, K., Nishimura, K., and Issler, D.: Seismic location and tracking of snow avalanches and slush flows on Mt. Fuji, Japan, Earth Surface Dynamics, 7, 989–1007, https://doi.org/https://doi.org/10.5194/esurf-7-989-2019, 2019.

Rosenfeld, A. and Pfaltz, J. L.: Sequential Operations in Digital Picture Processing, J. ACM, 13, 471–494, https://doi.org/https://doi.org/10.1145/321356.321357, 1966.

Schimmel, A., Hübl, J., McArdell, B. W., and Walter, F.: Automatic Identification of Alpine Mass Movements by a Combination of Seismic and Infrasound Sensors, Sensors, 18, https://doi.org/https://doi.org/10.3390/s18051658, 2018.

Schweizer, J., Jamieson, B., and Schneebeli, M.: Snow avalanche formation, Reviews of Geophysics, 41, https://doi.org/https://doi.org/10.1029/2002RG000123, 2003.

Simeon, A., Pérez-Guillén, C., Volpi, M., Seupel, C., and van Herwijnen, A.: Autoencoder-based feature extraction for the automatic detection of snow avalanches in seismic data, Geoscientific Model Development, 18, 8751–8776, https://doi.org/https://doi.org/10.5194/gmd-18-8751-2025, 2025.

Sovilla, B., Marchetti, E., Kyburz, M. L., Köhler, A., Huguenin, P., Calic, I., Kohler, M. J., Suriñach, E., and Pérez-Guillén, C.: The Dominant Source Mechanism of Infrasound Generation in Powder Snow Avalanches, Geophysical Research Letters, 52, e2024GL112 886, https://doi.org/https://doi.org/10.1029/2024GL112886, 2025.

Stoffel, M. and Huggel, C.: Effects of Climate Change on Mass Movements in Mountain Environments, Progress in Physical Geography: Earth and Environment, 36, 421–439, https://doi.org/https://doi.org/10.1177/0309133312441010, 2012.

Suriñach, E., Vilajosana, I., Khazaradze, G., Biescas, B., Furdada, G., and Vilaplana, J. M.: Seismic detection and characterization of landslides and other mass movements, Natural Hazards and Earth System Sciences, 5, 791–798, https://doi.org/https://doi.org/10.5194/nhess-5-791-2005, 2005.

Techel, F.: The Influence of Water on Snow: Micro-Structural Measurements and Wet Snow Stability Assessment, Masterarbeit, Philosophisch-naturwissenschaftliche Fakultät, Universität Bern, https://www.slf.ch/fileadmin/user_upload/WSL/Mitarbeitende/techel/techel_2010_influence_water_snow_stabiltiy_MSc_thesis-1.pdf, 2010.

Turquet, A., Wuestefeld, A., Kåre Nyhammer, F., Nilsen, E., and Refsum, V.: Advances in Avalanche Monitoring in Norway: Insights from Distributed Acoustic Sensing, in: European Geosciences Union General Assembly 2024 (EGU24), EGU General Assembly Conference Abstracts, p. 7603, https://doi.org/https://doi.org/10.5194/egusphere-egu24-7603, 2024.

Van Herwijnen, A. and Schweizer, J.: Seismic Sensor Array for Monitoring an Avalanche Start Zone: Design, Deployment and Preliminary Results, Journal of Glaciology, 57, 267–276, https://doi.org/https://doi.org/10.3189/002214311796405933, 2011.

Vilajosana, I., Khazaradze, G., Suriñach, E., Lied, E., and Kristensen, K.: Snow avalanche speed determination using seismic methods, Cold Regions Science and Technology, 49, 2–10, https://doi.org/https://doi.org/10.1016/j.coldregions.2006.09.007, selected Papers from the General Assembly of the European Geosciences Union (EGU), Vienna, Austria, 25 April 2005, 2007.

Walter, F., Gräff, D., Lindner, F., Paitz, P., Köpfli, M., Chmiel, M., and Fichtner, A.: Distributed acoustic sensing of microseismic sources and wave propagation in glaciated terrain, Nature communications, 11, 2436, https://doi.org/https://doi.org/10.1038/s41467-020-15824-6, 2020.

Withers, M., Aster, R., Young, C., Beiriger, J., Harris, M., Moore, S., and Trujillo, J.: A comparison of select trigger algorithms for automated global seismic phase and event detection, Bulletin of the Seismological Society of America, 88, 95–106, https://doi.org/https://doi.org/10.1785/BSSA0880010095, 1998.